A Comparison of Satellite Observations and Model Simulations of Column-Integrated Moisture and Upper-Tropospheric Humidity

C.-T. CHEN* AND ERICH ROECKNER

Max Planck Institute for Meteorology, Hamburg, Germany

BRIAN J. SODEN

NOAA/Geophysical Fluid Dynamics Laboratory, Princeton, New Jersey

ABSTRACT

Water vapor distributions obtained from the fourth generation ECHAM general circulation model are compared with satellite observations of total precipitable water (TPW) from the Special Sensor Microwave/Imager (SSM/I) and upper-tropospheric relative humidity (UTH) from TIROS-N Operational Vertical Sounder (TOVS). In general, the model simulations agree well with satellite observations of the climatological mean, seasonal variation, and interannual variation of moisture. There are, however, biases in the details. Underestimates in TPW and UTH are found off the west coast of continents, especially in the boreal summer over the eastern subtropical Pacific. These biases are related to both enhanced dry advection due to an excessively strong subtropical high and greater large-scale subsidence. A more intense tropical circulation in ECHAM4 is evidenced by the broadening of the high TPW and UTH zone that coincides with the equatorial convective regions. Additionally, interannual anomalies in equatorial UTH and TPW simulated by the model are found to be more sensitive to tropical SST anomalies than are the satellite data. The impact of changes in physical parameterizations upon the moisture distribution is also examined by comparing the simulations from the previous ECHAM3 and the current ECHAM4 models. The dry bias at the equator in ECHAM3 is related to the closure assumption used for deep convection, while the dry bias in UTH over the high-latitude winter hemisphere in ECHAM3 is a result of negative specific humidities produced by the spectral vapor advection scheme. With the new semi-Lagrangian advection scheme in ECHAM4, the simulated UTH over the same region becomes moister than TOVS observations suggest. The impact of discrepancies in the simulated water vapor distributions upon the radiation budget and cloud distribution in the model are also described.

1. Introduction

Water vapor is a key constituent of the earth's atmosphere (Chahine 1992). Its distribution, transport, and convergence determine cloud formation and precipitation, which affect agriculture and other human activities. The transformation of water between the various phases in the hydrological cycle and their interactions with convection, the large-scale circulation, and land surface processes are important for transferring energy within the earth–atmosphere system. Water vapor, being the primary greenhouse gas, profoundly modifies the radiative properties of the atmosphere, while clouds strongly regulate both the incoming solar and outgoing longwave radiation. In short, water vapor strongly influences climate on a variety of temporal and spatial scales. Consequently, an accurate simulation of climate requires proper treatment of the hydrological cycle.

It is realized that the most important mechanism to amplify the predicted global warming due to doubling of carbon dioxide is the water vapor feedback (Manabe and Wetherald 1967). Recently, it has been suggested that the changes in the upper-tropospheric moisture could significantly reduce the magnitude or even change the sign of the water vapor feedback (Lindzen 1990). Further, the distribution and supply of water vapor are the essential ingredients for our understanding of cloud distribution. Therefore, it is also crucial to the cloud feedback problem, which comprises the largest uncertainty and causes different climate sensitivities among various climate general circulation models (GCMs) (Cess et al. 1990). Proper assessment of moist processes is thus a fundamental requirement for understanding the climate change.

---
* Current affiliation: Department of Earth Sciences, National Taiwan Normal University, Taipei, Taiwan, R. O. C.

Corresponding author address: Dr. Cheng-Ta Chen, Department of Earth Sciences, National Taiwan Normal University, No. 88, Section 4, Ting-Chou Rd., Taipei 117, Taiwan, R. O. C.
E-mail: chen@atms.geos.ntnu.edu.tw

Despite the importance of water vapor in the climate system, studies on the validation of water vapor climatology in atmospheric GCMs are limited. Part of the reasons can be attributed to the poor treatment of vapor advection and uncertainties in formulating the source/sink of water vapor (Williamson and Rasch 1994; Browning 1994; Miller et al. 1992). Though considerable efforts have been undertaken to construct a water vapor climatology using data from the global radiosonde network (e.g., Oort 1983; Gaffen et al. 1991), the constraints of radiosonde observations are still large. In particular, there are problems over the ocean, where the radiosonde network is sparse, and in the upper troposphere where the radiosonde humidity sensor is considered unreliable (Chahine 1992). Fortunately, the extensive satellite archives obtained in recent years provide alternative data sources for the water vapor with near-global coverage.

Soden and Bretherton (1994) used satellite observations to evaluate the spatial and temporal variations of total precipitable water (TPW) and upper-tropospheric humidity from analyses of the European Centre for Medium-Range Weather Forecasts (ECMWF) and the simulation of the Community Climate Model (CCM) of the National Center for Atmospheric Research. In their study, the retrieval of TPW is from the Special Sensor Microwave/Imager (SSM/I) launched in 1987 on the operational spacecraft of the Defense Meteorological Space Program. It is considered more accurate than the retrieval from the previous microwave and infrared sensors (Liu et al. 1992). The 6.7 μm brightness temperature ($T_{6.7}$) from GOES is used as an indication for upper-tropospheric moisture (Soden and Bretherton 1993). The ability of these models in simulating the primary features of the water vapor distribution is highlighted in their investigation. In this study, we follow the above comparison with emphasis on the validation of the water vapor climatology and interannual variability from a long-term climate simulation using the fourth generation atmospheric GCM developed at the Max Planck Institute for Meteorology in Hamburg (ECHAM4). The satellite data used in this study and the characteristics of the ECHAM4 are described in section 2. The comparison of the annual mean and seasonal variation of column-integrated water vapor is presented in section 3. The mean and variability of the upper-tropospheric humidity inferred from satellite observations and model outputs are presented in section 4. In section 5, we briefly illustrate the impact of tropical sea surface temperature (SST) anomalies on total and upper-tropospheric water vapor abundance shown in both satellite and model results. Section 6 examines the difference in water vapor distribution in ECHAM4 and the previous generation model, ECHAM3. The comparison highlights the impact of changes in physical parameterizations on the water vapor distribution in two models. The influences of water vapor distribution simulation on the model's

energy budget and cloud distribution are briefly discussed in section 7. Section 8 summarizes the findings.

2. Data

a. Satellite

1) SSM/I TPW

The TPW retrieval algorithm is described in Liu et al. (1992). The rms difference between the SSM/I retrieval and colocated radiosonde observations is 3.1 kg m^{-2} with no systematic bias (Liu et al. 1992) and is similar to that derived using the National Environmental Satellite Data and Information Service (NESDIS) algorithm (Alishouse et al. 1990). Microwave TPW observations are generally considered to provide the best global measurements available and have the advantage of providing retrievals under cloudy conditions. However, TPW is not retrieved over land- and ice-covered ocean due to the large variation in surface emissivity. Monthly mean TPW observations from July 1987 to June 1991 (no data in December 1987) are used in this study. An ensemble average of TPW for the June, July, August (JJA) and December, January, February (DJF) seasons and annual mean are derived from the monthly mean data.

2) TOVS $T_{6.7}$

This study uses clear-sky radiances from the TIROS-N Operational Vertical Sounder (TOVS) on the NOAA operational polar-orbiting satellite to describe the distribution of upper-tropospheric moisture. Compared with similar measurements available from GOES and Meteosat, TOVS provides a better global coverage and long temporal span. Channel 12 (6.7 μm) of High-Resolution Infrared Radiation Sounder (HIRS) unit in the TOVS package is designed to sense the amount of water vapor in the upper troposphere. The sensitivity of HIRS channel 12 for a typical tropical profile at nadir viewing is greatest between 200 and 500 mb (Fig. 1 in Wu et al. 1993). Detailed error analyses are given in Wu et al. (1993). The overall error from instrument noise, angular correction, and cloud clearing for the brightness temperature at channel 12 is about 1 K for each pentad bin with five observations. The random error from monthly mean products can be even smaller. One disadvantage for this dataset is that the data is subject to clear-sky sampling bias. The magnitude of this bias is difficult to estimate, although recent comparisons with radiosonde climatologies suggest that it is less than 1 K (Soden and Lanzante 1996).

The procedure for validating the distribution of upper-tropospheric water vapor simulated by a GCM is to compare the observed clear-sky $T_{6.7}$ with that calculated by a radiative transfer model using GCM profiles of temperature and moisture as input. In this study, the University of Wisconsin—Operational TOVS

Transmittance Model (OTTM) is used to perform the $T_{6.7}$ calculation. The OTTM is a 40-level, multivariate regression model based on line-by-line transmittance calculations (Weinreb et al. 1981). The uncertainty in the calculated brightness temperature is estimated to be approximately 1.5–2.0 K (Soden and Lanzante 1996). One should also keep in mind that the different clear-sky sampling in the model can lead to a wetter upper troposphere as compared to that in the satellite retrievals. The annual, seasonal, and monthly means of $T_{6.7}$ are derived from ensemble averages from all monthly mean data between 1981 and 1989.

b. Model

TPW is taken directly from the model output and $T_{6.7}$ is calculated from model temperature and moisture profiles using the OTTM referred to in the previous section.

The fourth generation atmospheric GCM at the Max Planck Institute for Meteorology incorporates the most recent improvements in physical representation of a wide range of key climate processes in the ECHAM model series. Cloud/radiation, moisture transport, convection, cloud-turbulence interaction in the planetary boundary layer and land surface data are the major processes that have been revised. These changes have strengthened the model's performance in climate simulation. A detailed description of the dynamical and physical structure, and the simulated climatology of the ECHAM4 is documented by E. Roeckner et al. 1995, personal communication. The main characteristics of the model are highlighted as follows:

The prognostic variables in the model include vorticity, divergence, temperature, surface pressure, water vapor, and cloud water. This study examines simulations with T42 resolution and 19 hybrid vertical levels in which semi-implicit, leapfrog time integration with a 24-min time step is used. A new radiation code (Fouquart and Bonnel 1980; Morcrette 1991) replaces the old radiation scheme (Hense et al. 1982) in ECHAM3. There are the following further modifications in the new code: (i) additional greenhouse gases (CH_4, N_2O, CFCs, and 14.6-μm O_3 band) are included; (ii) the single scattering properties of cloud water droplets and ice crystals are parameterized according to Rockel et al. (1991). The effective radii of cloud droplets and ice crystals are parameterized from the liquid/solid water content, (iii) water vapor continuum is modified to include temperature weighted band averages of e-type continuum absorption and band dependent ratio of (p-e)-type to e-type continuum absorption (Giorgetta and Wild 1995).

It is known that the moisture field exhibits large horizontal and vertical spatial variability and that there are small-scale sources and sinks of moisture associated with phase changes. Thus, although the spectral transform method is useful for approximating large-scale,

global atmospheric dry dynamics, it is less successful in handling water vapor (Rasch and Williamson 1991; Williamson and Rasch 1994). One of the major changes from ECHAM3 to ECHAM4 is that a semi-Langrangian transport method (Williamson and Rasch 1989) replaces the spectral method for the advection of moisture and cloud water.

The vertical turbulent transfer of momentum, heat, water vapor, and cloud water is based on the Monin–Obukhov similarity theory for the surface layer and the eddy diffusivity approach above the surface layer (Louis 1979). The drag and heat transfer coefficients depend on roughness length and Richardson number, and the eddy diffusion coefficients depend on wind shear, mixing length, and Richardson number, which has been reformulated using cloud-conservative variables (Brinkop and Roeckner 1995). The first-order turbulence closure scheme in ECHAM3 is replaced by a turbulent kinetic energy closure with the Prandtl–Kolmogorov parameterization of eddy diffusivity (Brinkop and Roeckner 1995).

A mass flux scheme for deep, shallow, and midlevel convection is employed (Tiedtke 1989) except that the closure for penetrative convection is reformulated to account for moisture convergence dependence on convective instability (CAPE) (Nordeng 1994). Cumulus clouds are represented by a bulk model including the effect of entrainment (organized and turbulent) and detrainment (mostly through organized outflow at cloud top) on the updraft and downdraft convective mass fluxes. Organized entrainment depends on local buoyancy and organized detrainment is derived for a spectrum of clouds (Nordeng 1994).

The prediction of stratiform clouds is based on the cloud water transport equation including sources and sinks due to condensation/evaporation, and precipitation formation by coalescence of cloud droplets and sedimentation of ice crystals (Sundquist 1978; Roeckner et al. 1991). Evaporations of cloud water and precipitation are considered. Subgrid-scale condensation and cloud formation is taken into account by specifying height-dependent thresholds of relative humidity (Xu and Krueger 1991; Walcek 1994). The same threshold is applied to both convective and stratiform cloud. The detrained fraction of the convectively generated cloud water is coupled with the stratiform (anvil) cloud water equation.

A new global dataset of land-surface parameters is used (Claussen et al. 1994). These parameters (surface background albedo, surface roughness length, leaf area index, fractional vegetation cover, and forest ratio) are constructed from the major ecosystem complex of Olson et al. (1983). The land surface parameterization comprises the budgets of heat and water in the soil, the snow pack over land and the heat budget of permanent land ice and sea ice (Dümenil and Todini 1992). The heat transfer equation is solved in a 5-layer model with zero heat flux at the bottom. Soil moisture, vegetation,

and snow are the three reservoirs for the water budget equation. Vegetation effects such as interception of rain and snow in the canopy and stomatal control of evapotranspiration are parameterized (Blondin 1989). The runoff scheme is based on catchment considerations and takes into account subgrid-scale variations of field capacity over inhomogeneous terrain.

The model has been integrated with the monthly observed SST and sea ice for the period 1979–1988 from the so-called Atmospheric Model Intercomparison Project (AMIP) dataset (Gates 1992). Means and variability of TPW and $T_{6.7}$ are derived from the ensemble monthly mean temperature and moisture profiles of the 10-year integration unless mentioned elsewhere.

3. Column-integrated water vapor

The global, annual-mean distribution of TPW from SSM/I, ECHAM4, and the differences are shown in Fig. 1. Comparison is restricted to the region equatorward of 60° since the retrievals over ice are less reliable. The standard deviations of annual mean TPW from ECHAM4 (10-year integration) are shown in Fig. 2. They reveal the interannual variability in the model. The maximum standard deviation is found in the tropics, especially in the central equatorial Pacific where the typical value is 3–4 kg m^{-2}. This can be expected from the large SST anomalies associated with El Niño events in the equatorial region and the close relationship between SST and TPW (Stephens 1990). The values of interannual variability are normally less than 1 kg m^{-2} in the extratropics. Unfortunately, the SSM/I observational records are too short to evaluate the observed variability. In the later comparisons between satellite observation and model simulations, we focus on the discrepancies that are greater than the model's variability.

The seasonal distribution of TPW from SSM/I in 1987 and 1988 are described in Liu et al. (1992) and Soden and Bretherton (1994). Here we show the annual average from the 4-year data (Fig. 1a). The observed TPW fields from SSM/I are essentially zonal in nature, although variations along the latitude circle, generally associated with particular surface and large-scale circulation features, are apparent. In the Tropics, there are variations related to gradients of sea surface temperature and, hence, evaporation. For example, the dry tongues along the west coasts of the continents are related to cold SST induced by ocean upwelling (Gaffen and Barnett 1992). The large-scale atmospheric subsidence of dry air in these regions further suppresses the water vapor abundance. The maximum TPW between 0° to 10°N along the latitude cycle and the southeastward extension from Indonesia toward the southern Pacific indicates the location of the intertropical convergence zone (ITCZ) and South Pacific convergence zone (SPCZ), respectively. The equatorial western Pacific warm pool region and eastern Indian Ocean also

persistently reveal greater TPW. The warmer SST and large-scale moisture convergence are the principle processes to enhance the TPW over these areas. Lower TPWs are found in the midlatitudes, which is to be expected from the latitudinal SST gradient and the relationship between temperature and saturation vapor pressure dictated by the Clausius–Clapeyron equation.

The annual means in TPW fields from ECHAM4 (Fig. 1b) capture most of the features described in the SSM/I observations. The location of the ITCZ and SPCZ, the Pacific warm pool, and the extent of the dry tongues off the west coasts of the continents are well simulated. Despite the overall good agreement, there are some systematic errors in TPW (Fig. 1c). The dry tongue in the eastern subtropical ocean basins extend slightly more equatorward than SSM/I data suggest. On the other hand, in the western part of the ocean basins the simulation generally has larger TPW than that of SSM/I. The comparison of mean sea level pressure from ECMWF analyses and ECHAM4 suggests the moisture advection associated with the stronger subtropical high in the summer hemisphere being one of the reasons for this east–west discrepancy in TWP over the ocean basins. In addition, the simulated zonal mean westerlies in the upper troposphere over the tropical region as opposite to the ECMWF analyses, suggesting an overestimate in the strength of the Walker circulation. Thus, an enhanced large-scale subsidence off the west coast of continents in the summer hemisphere in the ECHAM4 also serves to suppress the transport of water vapor from the boundary layer into the free atmosphere. Similar discrepancies were also noted recently by Soden and Bretherton (1994) for a comparison between SSM/I observation and CCM2 simulation. The maritime continent and northern Indian Ocean tend to have smaller TPW. They are related to a slight difference in the geographical locations of the simulated convective centers and east–west longitudinal circulation in the Tropics. Thus, the ITCZ and SPCZ east of the date line and the western Indian Ocean, on the contrary, have higher TPW.

Figure 3 illustrates the annual cycle of the zonal mean oceanic TPW from SSM/I, ECHAM4, and the differences, respectively. Both the observations and simulations depict a maxima in TPW, which follows the seasonal migration of the ITCZ. The model shows a tropical maximum of TPW from July to September at 10°N, while the SSM/I data indicate a longer period of TPW maximum between April and October. The larger seasonal cycle of TPW in the Northern Hemisphere is evident in both the ECHAM4 and SSM/I data. Differences between ECHAM4 and SSM/I include a moist bias over the Southern Hemisphere subtropics during the austral summer, a Northern Hemisphere subtropical dry bias during the boreal summer, and a winter to spring dryness near the equator. While the underestimate in TPW over the equatorial Atlantic Ocean and Indonesia is primarily responsible for the
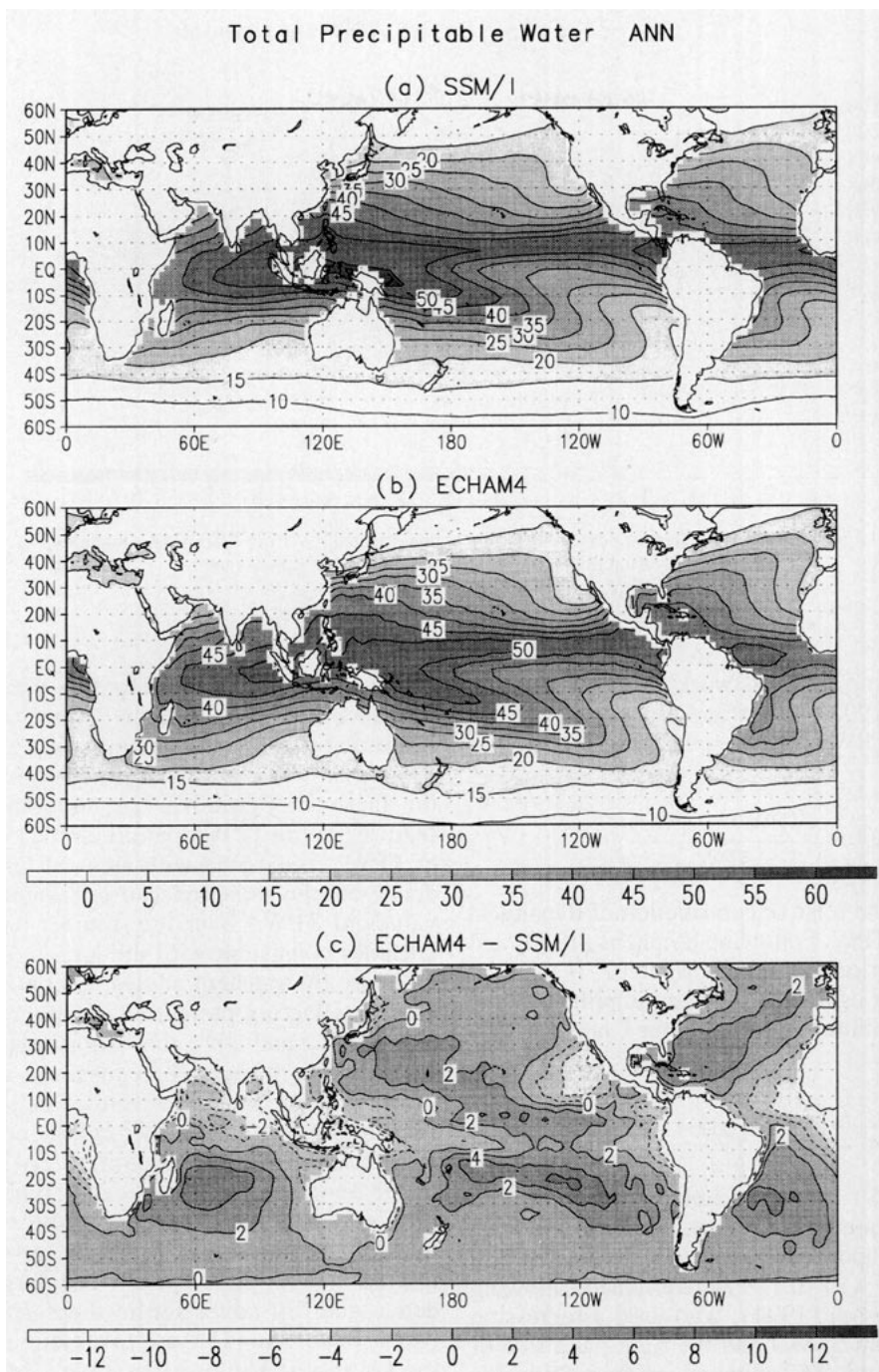
FIG. 1. Geographic distribution of the annual mean TPW from (a) SSM/I, (b) ECHAM4, and (c) the difference ECHAM4-SSM/I. Units are kilograms per square meter.

equatorial dryness in winter, dry biases over the Bay of Bengal and Arabian Sea are more responsible for the discrepancies in spring. Although these differences are within the rms accuracy of the measurements, they are very systematic suggesting that they represent deficiencies in the model or a systematic error in the TPW retrieval for these particular regions.

Since the saturation water vapor pressure depends on the temperature through the Clausius–Clapeyron relationship, the main pattern of TPW reflects the thermodynamic dependence upon SST (prescribed in the model run). It is, therefore, more informative to illustrate the dynamical impact on the TPW using the available data. For this purpose, we use a normalized TPW
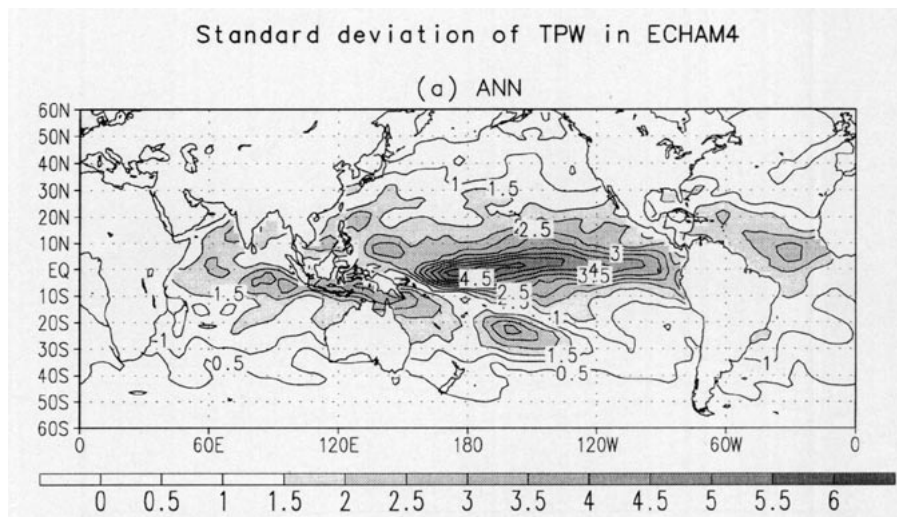
FIG. 2. Interannual standard deviation of the annual mean TPW from ECHAM4 simulations (10-year integration). Units are kilograms per square meter.

parameter following previous work (Prabhakara et al. 1979; Stephens 1990; Soden and Bretherton 1994). The normalized TPW parameter, TPW*, is defined as follows:

$$TPW* = \frac{(TPW - TPW')}{TPW}, \qquad (1)$$

which measures the relative contribution of dynamical influences to the TPW. Following Stephens (1990) and Soden and Bretherton (1994), TPW' in (1) is the total precipitable water estimated using a simplified model based on an approximate version of the Clausius–Clapeyron equation:

$$TPW' = 10.82 \frac{r}{(1 + \lambda)} \exp[0.064 \, (T_s - 288)], \quad (2)$$

where T_s is the SST, r is the relative humidity, and λ is the ratio of the atmospheric scale height to the scale height of water vapor and has a typical value of 3.5. The factor $r/(1 + \lambda) = 0.178$ is determined following Soden and Bretherton (1994), who used a regression between TPW from SSM/I and the right-hand side of (2) using the monthly SST climatology from Reynolds (1982).

To examine the seasonal variations, we show TPW* to emphasize influences from the large-scale circulation. Figures 4 and 5 illustrate the geographical distribution of seasonal mean TPW*, expressed as percentage, from SSM/I observation, ECHAM4 simulation, and their differences for the JJA and DJF seasons, respectively. The positive TPW* means a greater than average moisture abundance for a specific SST. Thus, it is likely to be located in regions with moisture convergence or moist air advection.

On the other hand, the negative value suggests the influence of subsidence or dry air advection. Both observation and model simulation show similar distributions of TPW*, which highlight the impact of the large-scale atmospheric motions. The primary features in the TPW* pattern are (i) negative values of TPW* associated with areas of large-scale subsidence off the west coast of continents, (ii) positive values of TPW* over the summer hemisphere mid-latitudes consistent with the large northward flux of moisture by transient eddies, (iii) positive values of TPW* reflecting moisture convergence in the ITCZ and SPCZ, and (iv) the large negative values of TPW* over the winter hemisphere associated with the descending branch of Hadley cell and dry air advecting out from the colder continent.

Although ECHAM4 qualitatively simulates most of the above features, there are some discrepancies in the details. An advantage in the analyses here is that we gain more insight in the processes that are related to the differences. The large-scale subsidence and dry advection in the eastern subtropical North Pacific for JJA are overestimated and extend too far south. The positive TPW* in the ITCZ during JJA is slightly weakened by this extension. There is also a small dry bias off the coast of northwestern Africa. The problems in simulating the large-scale subsidence and the strength of the dry advection controlled by the subtropical high described previously are likely to be responsible for these biases. In DJF, the large-scale moisture convergence in the Tropics is stronger over the central Pacific and Indian Ocean in ECHAM4 instead over the western equatorial Pacific warm pool and eastern Indian Ocean as in SSM/I. Consequently, a dry
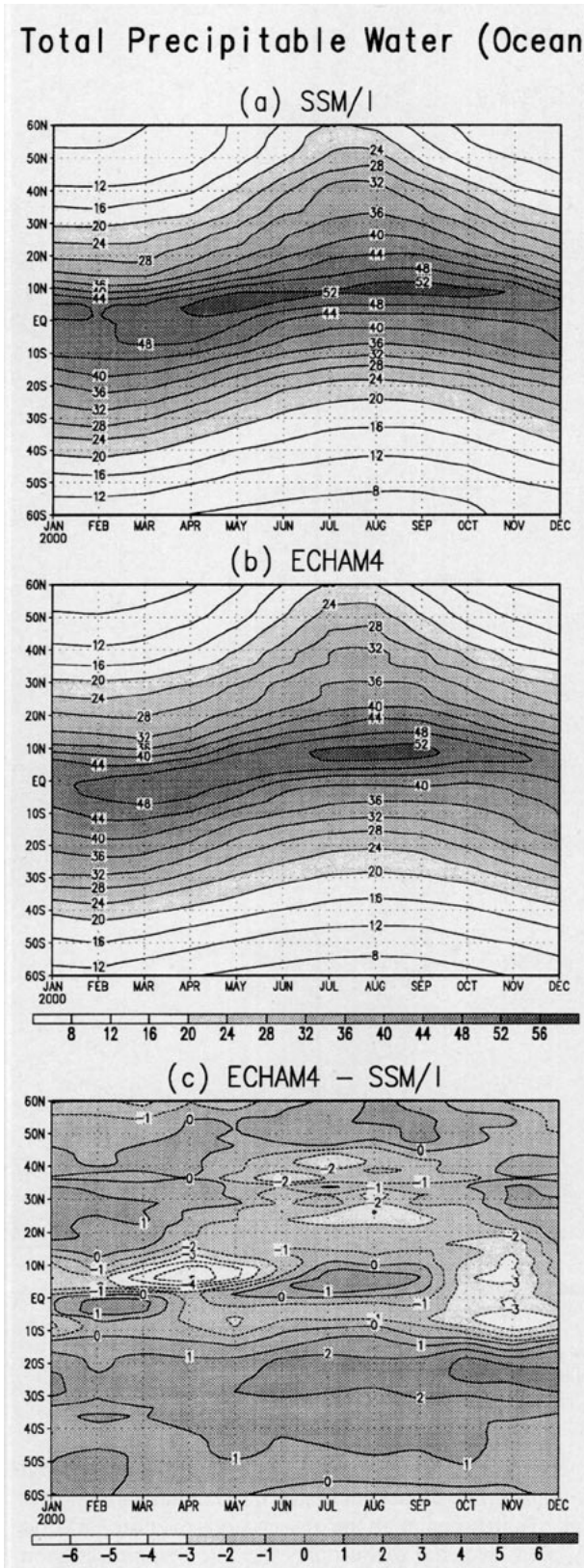
Total Precipitable Water (Ocean

(a) SSM/I

(b) ECHAM4

8 12 16 20 24 28 32 36 40 44 48 52 56

(c) ECHAM4 − SSM/I

−6 −5 −4 −3 −2 −1 0 1 2 3 4 5 6

FIG. 3. Latitude–month distribution of the zonal mean TPW over the ocean from (a) SSM/I, (b) ECHAM4, and (c) the difference ECHAM4-SSM/I. Units are kg m^{-2}.

bias is found near Indonesia. Over the equatorial Atlantic Ocean, the convergence in the model is too weak, resulting in an underestimate of TPW*. On the other hand, the convergence off the coast of southern Brazil toward the southeast is stronger than in the SSM/I observation. An overestimate of TPW* along a band extending from the warm pool toward the southern Pacific is also evident. The positive TPW* in the midlatitude summer hemisphere in ECHAM4 suggests an overestimate of moisture transport from low latitudes by transient eddies, whereas the less negative TPW* in the winter hemisphere implies that air advected from continents moister than SSM/I observations suggest. Although we discuss the processes linked to the model biases in a simple and direct manner, one should be reminded that the interactions between water vapor distribution and physical processes are complex and sensitive to other model biases (e.g., temperature, radiation, cloud). The representation of slantwise and midlevel convection, common in midlatitude storm systems, and their relation to the water vapor distribution also need further studies.

4. Moisture in the upper troposphere

Since the mass of water vapor is concentrated mainly within the first few kilometers above the ocean surface, the distribution of TPW primarily reflects moisture in the lower troposphere (Prabhakara et al. 1979). We have mentioned already the importance of the upper-tropospheric moisture in determining the amount of longwave radiation trapped by the atmosphere and its implication for climate simulation. The upper-tropospheric humidity is also important for simulating the formation and dissipation of high cirrus cloud, which also modifies the outgoing longwave radiation.

Here we use the $T_{6.7}$ measured from TOVS and calculated $T_{6.7}$ using the monthly mean temperature and moisture profiles from the model's 10-year integration as an indicator for the moisture amount in the upper troposphere.

The geographical distribution of the annual mean $T_{6.7}$ from TOVS observation and ECHAM4 simulation is compared in Fig. 6. The $T_{6.7}$ monthly climatology is described in Wu et al. (1993). Here we iterate the major features from our ensemble annual average. The $T_{6.7}$ is primarily sensitive to relative humidity vertically averaged over a range of pressures in the upper troposphere [mainly between 200 and 500 hPa; see Fig. 1 in Wu et al. (1993)]. A higher $T_{6.7}$ indicates a drier upper troposphere unless there is a substantial temperature increase, whereas a lower $T_{6.7}$ indicates a more moist upper troposphere. Note that the sensitivity of $T_{6.7}$ is roughly 5 to 8 times more sensitive to variations in relative humidity than to variations in temperature (Soden and Bretherton 1993). Figure 7 shows the inter-
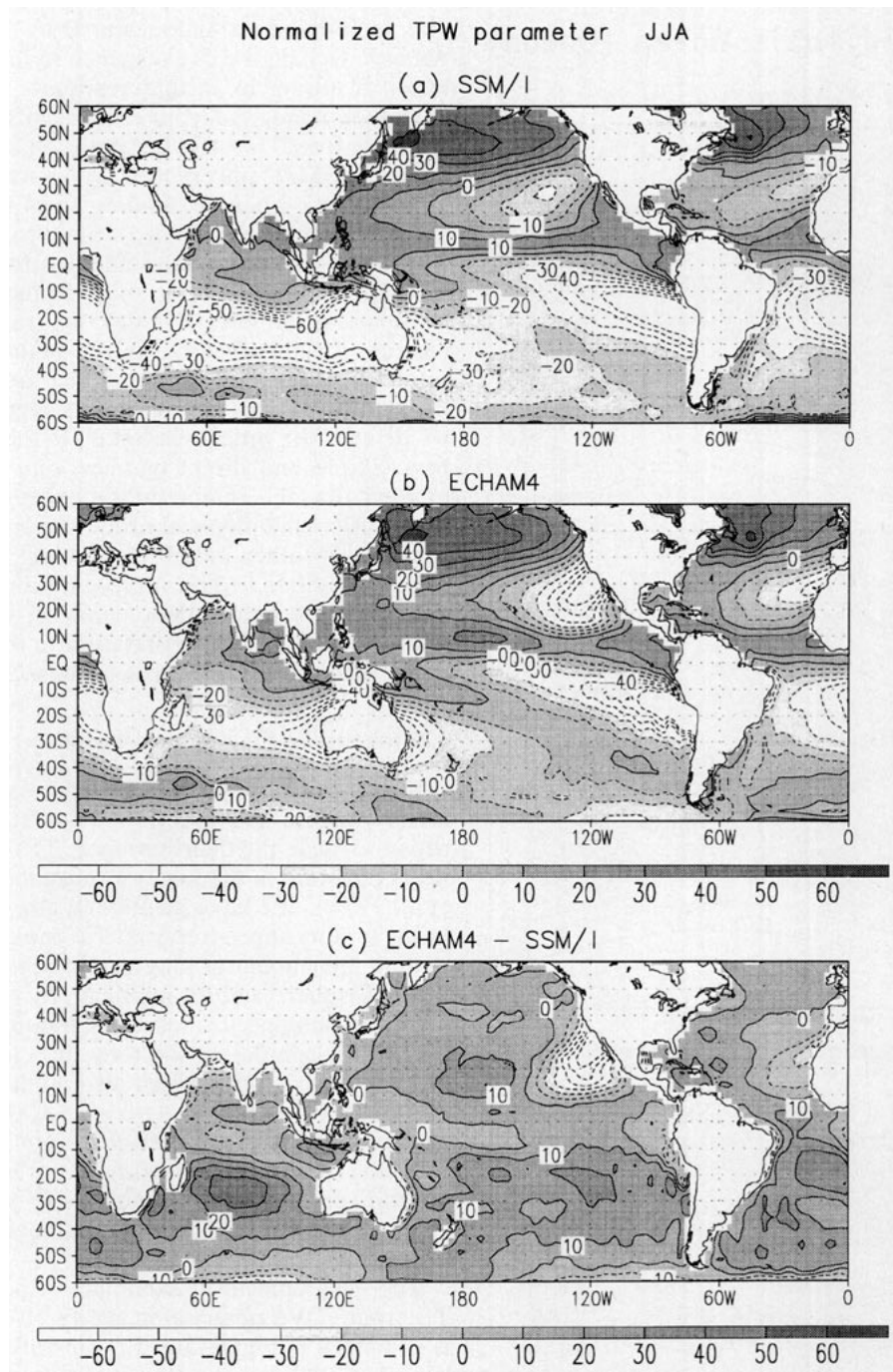
FIG. 4. Geographic distribution of the JJA seasonal mean TPW* from (a) SSM/I,
(b) ECHAM4, and (b) the difference ECHAM4-SSM/I. Units are percent.

annual standard deviation of the annual mean $T_{6.7}$ from ECHAM4 (10-year integration) and TOVS (1981–1989). The interannual variation of the upper-tropospheric moisture abundance in the model is greater in the Tropics than in the extratropics. The maximum values found in the central equatorial and eastern subtropical Pacific are over 1.5 K. Again, in the later comparison, we

focus on model biases that are larger than the interannual variability. The model simulated interannual variability is in good agreement with the observations over the Tropics; however, over the extratropics the interannual variation is smaller than observed.

The observed upper troposphere is relatively dry in areas corresponding to the descending branch of the

Normalized TPW parameter   DJF

(a) SSM/I

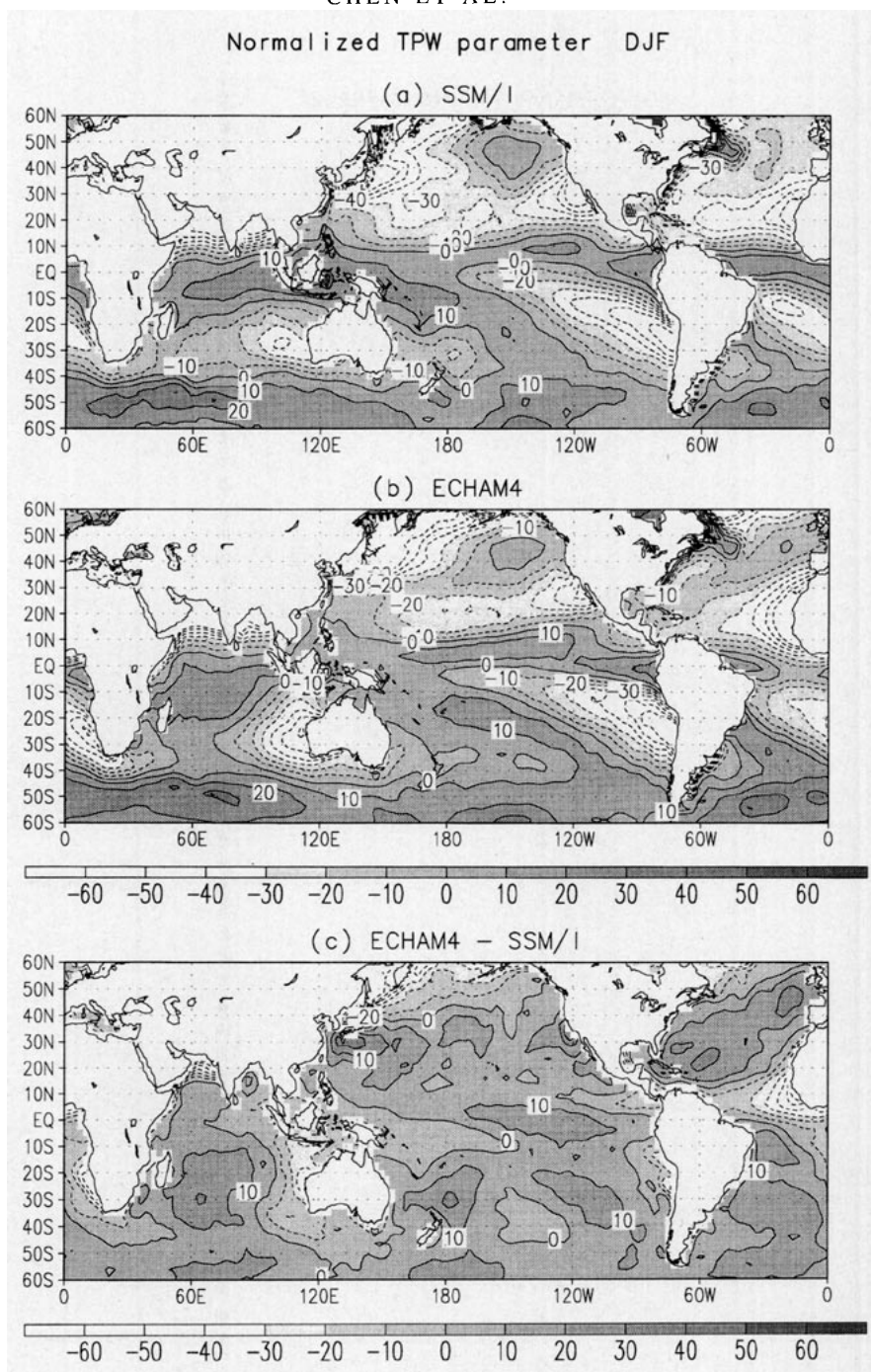### (b) ECHAM4

(c) ECHAM4 — SSM/I

FIG. 5. As in Fig. 4 except for the DJF season.

Hadley circulation and large-scale subsidence regions off the west coast of continents (Fig. 6a). Higher $T_{6.7}$ are especially pronounced between 10° and 20°S from the eastern Atlantic through the Indian Ocean and the eastern Pacific off Peru. High $T_{6.7}$ values are also found over the central Pacific and Atlantic between 10° and 20°N. There is another maximum over the northern Arabian Peninsula, which is likely related to strong subsidence over that region as indicated by ECMWF analyses. The convective centers over the Pacific warm pool and eastern Indian Ocean and also over the Amazon and Congo River basins can be identified by the relatively low $T_{6.7}$. It is evident that the upper-tropospheric humidity is related to penetrative convection. Vertical transport triggered by convection is the primary source of upper-tropospheric moisture in the
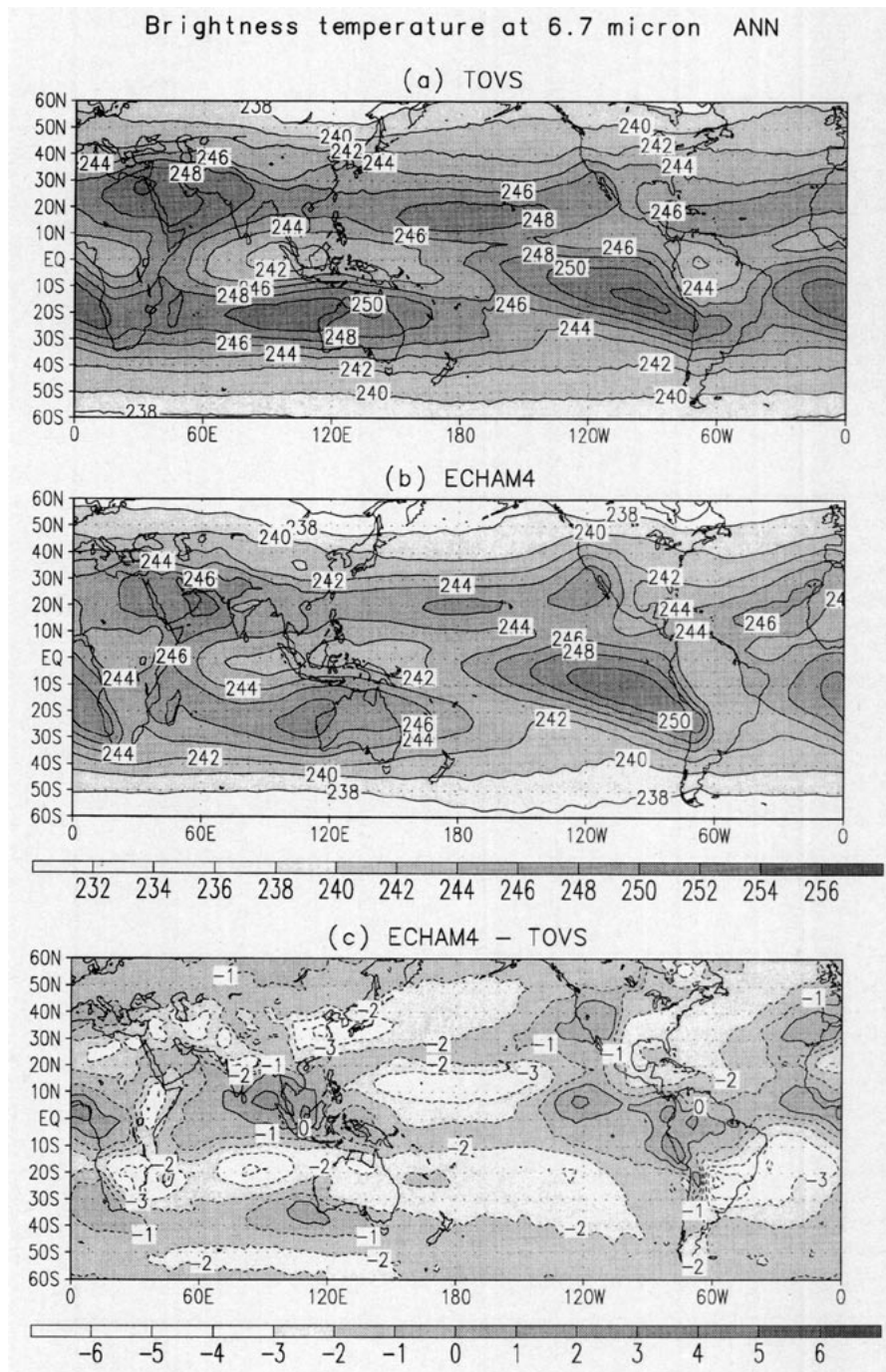
FIG. 6. Geographic distribution of the annual mean $T_{6.7}$ from (a) TOVS, (b) ECHAM4, and (c) the difference ECHAM4-TOVS. Units are kelvins.

Tropics (Lohmann et al. 1995). It has also been argued that upper-level clouds associated with convective updrafts are the major moisture source for the upper troposphere (Sun and Lindzen 1993). The locations of deep convective clouds categorized by the International Satellite Cloud Climatology Project (ISCCP; Rossow and Lacis 1990) coincide well with the low $T_{6.7}$ centers.

However, the formation and dissipation of convective updrafts and tropical cloud clusters, the associated precipitation processes, and how they relate to the moisture amount in the upper troposphere are still areas of further research (Betts 1990; Sun and Lindzen 1993; Soden and Fu 1995). There are also low $T_{6.7}$ in the midlatitudes. The lower-atmospheric temperature, the
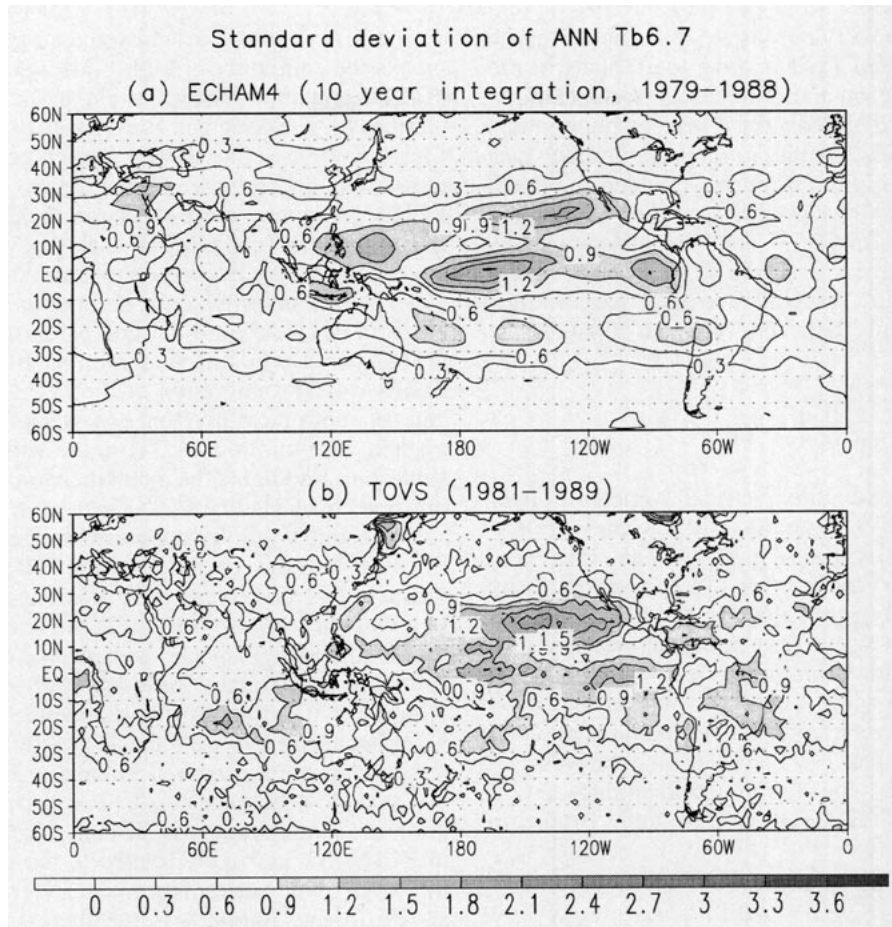
FIG. 7. Interannual standard deviation of the annual mean $T_{6.7}$ from (a) ECHAM4 (10-year integration, 1979–1988) and (b) TOVS (1981–1989). Units are kelvins.

vertical moisture transport, and the reevaporation from the upper-level clouds generated by the midlatitude synoptic systems are all likely candidates to explain the low values here.

ECHAM4 qualitatively reproduces the annual mean pattern of the extrema in $T_{6.7}$ (Fig. 6b). However, there are some discrepancies. The large-scale subsidence off the west coast of North America and in the eastern subtropical Atlantic produces a drier upper troposphere than TOVS observations indicate. This is consistent with the problem of excessive large-scale subsidence over those areas in ECHAM4 also noted in the TPW comparison. Other dry biases in the equatorial region are also closely related to the location of dry biases in TPW. The range of the moist area ($T_{6.7} < 244$ K) in the equatorial convective centers in ECHAM4 is larger than that from TOVS and the southeastward extensions of low $T_{6.7}$ from the Pacific warm pool and Amazon River basin in ECHAM4 are also more pronounced. Cold biases of $T_{6.7}$ in the model are also found over the central Pacific near 10°N, over southern Brazil toward the Atlantic Ocean, over the subtropical Indian Ocean

toward southern Africa, and in the two major storm tracks in the Northern Hemisphere.

It should be noted that the observed $T_{6.7}$ could have a systematic bias due to clear-sky (dry) sampling. However, the observed $T_{6.7}$ values in the Tropics could be subject to cloud contamination, which would lower the $T_{6.7}$. Detailed error analyses are required to quantify these influences. For the subtropics, less sampling bias is introduced since upper-level clouds over these regions are rare. Another source of error is the use of monthly mean temperature and moisture profiles from the model to derive $T_{6.7}$. Since the mean $T_{6.7}$ from TOVS is constructed from daily measurements, it would be more appropriate to use the daily temperature and moisture profiles from the model to obtain mean $T_{6.7}$. A simple error analyses on a few selected months shows that the use of monthly mean temperature and moisture profiles could introduce a cold bias. This cold bias is small, mostly ranging from <0.5 K in the Tropics and <1 K in the extratropics. Additionally, the patterns of $T_{6.7}$ are not sensitive to the use of monthly mean temperature and moisture profiles.

Although it is more appropriate to compare the observed and simulated $T_{6.7}$'s in order to evaluate the model's performance on the simulation of upper-troposphere water vapor abundance, it is conceptually more clear if one can relate the $T_{6.7}$ to a more familiar measure of water vapor. For this purpose, Soden and Bretherton (1993, 1994) developed a simplified treatment of the radiative transfer at 6.7 μm, which demonstrated that, accurate to about 1 K, the $T_{6.7}$ can be related to the relative humidity vertically averaged over the upper troposphere (mainly between 200 and 500 hPa) according to

$$\log\left(\frac{\text{UTH}p}{\cos\theta}\right) = (a + b)T_{6.7}, \qquad (3)$$

where UTH is the weighted vertical average of upper-tropospheric relative humidity, p is the pressure at T = 240 K divided by 300 hPa, θ is the satellite zenith angle, and $a = 31.5$ and $b = -0.114$ K^{-1} are regression coefficients. The typical value for p range from 0.9 to 1.5. The θ here is set to zero since the radiance measured by TOVS are "limb corrected" to produce the equivalent "nadir view" radiance (Wu et al. 1993). The above formula is used to convert both the observed and model-simulated $T_{6.7}$ to UTH. One can also use (3) to relate the $T_{6.7}$ bias to the fractional difference in UTH [e.g., ΔUTH/UTH; Soden and Bretherton (1994)]:

$$\frac{\Delta\text{UTH}}{\text{UTH}} = b\Delta T_{6.7}. \qquad (4)$$

Thus, a $T_{6.7}$ bias of 2 K corresponds to a fractional error in UTH of roughly $(0.114)(2) \approx 0.23$; that is, for a UTH of 50% this would correspond an error in UTH of $(0.23)(50\%) \approx 11\%$.

For the seasonal variation of the upper-tropospheric humidity distribution, we illustrate the results in terms of UTH as derived from (3) using $T_{6.7}$. Figures 8 and 9 illustrate the geographical distribution of seasonal mean UTH from TOVS observation, ECHAM4 simulation, and their differences for the JJA and DJF seasons, respectively. The primary spatial patterns in UTH reflect those noted for $T_{6.7}$. Areas of frequent deep convection, such as Central America and Africa, tend to have greater UTH in both model and observation, whereas areas of large-scale subsidence have smaller UTH. The seasonal migration of convective centers from Central America to Brazil, from Sahel to the Congo River basin, and from the Bay of Bengal to the north of Australia are also apparent in the UTH maps. Both the model and observations also indicate the seasonal movement of the subtropical dry bands following the shift of the downward branch of the Hadley circulation. High values of UTH are also noted over the storm tracks, although the model tends to overestimate the UTH here in both seasons. ECHAM4 also underestimates the UTH off the west coast of North America

during JJA resulting in an expanded dry band, which breaks the continuity of high UTH associated with the ITCZ. Compared to other recent studies on UTH simulations (e.g., Soden and Bretherton 1994; Salathé and Chesters 1995), the slightly larger contrast between moist and dry regions of the upper troposphere in ECHAM4 appears more similar to the CCM simulation as compared to the ECMWF analyses, which exhibited a weaker contrast between moist and dry regions.

To further investigate the simulation of the seasonal cycle in UTH. Figure 10 compares the zonal mean UTH evolving in different months from TOVS and ECHAM4. The migration of the ITCZ (higher UTH) and the subtropical dry zones (lower UTH) are clearly evident. The minimum UTH in the winter hemisphere subtropics highlights the intensification of the descending branch of Hadley cell. There is a lag behind the solar heating cycle by approximately two months coinciding with the migration of the ITCZ (Waliser and Gautier 1993). The seasonal variations of UTH in midlatitudes are larger in the Northern Hemisphere than in the Southern Hemisphere, as expected from the corresponding temperature variations and associated baroclinic activity. Figure 10c shows the differences in UTH between ECHAM4 and TOVS. While the general temporal evolution is well simulated in the model, a few notable differences exist. The slightly broader latitudinal extent of higher UTH in the Tropics is apparent in ECHAM4 and likely related to the overestimate of the range of the convergence zone. This is most clearly shown in the Southern Hemisphere from November through February when the SPCZ is formed. Recent studies (Hess et al. 1993; Slingo et al. 1994) have also illustrated the broad latitudinal extent of the mean meridional circulation associated with the Kuo-type and Tiedtke schemes. ECHAM4 also shows a systematic wet bias in the zonal mean UTH over midlatitudes. Although we note that the cold bias in the upper troposphere at higher latitudes in ECHAM4 may partly contribute this by causing and underprediction in $T_{6.7}$, which may be erroneously intepreted as excessive relative humidity. We also note that the TOVS observations in the extratropics may be affected by a clear-sky (dry) sampling bias.

5. Effect of SST anomaly on the water vapor distribution

The close relationship between SST and TPW is illustrated by Stephens (1990). Gaffen et al. (1991) also demonstrated that the specific humidity variations in the Tropics and globally seem to be related to the El Niño–Southern Oscillation (ENSO) cycle. Here we investigate the impact of tropical SST anomalies on the circulation and resulting TPW and UTH as indicated in satellite observations and model simulation. As part of the present model evaluation work, the ability of the model in reproducing the TPW and UTH distribution
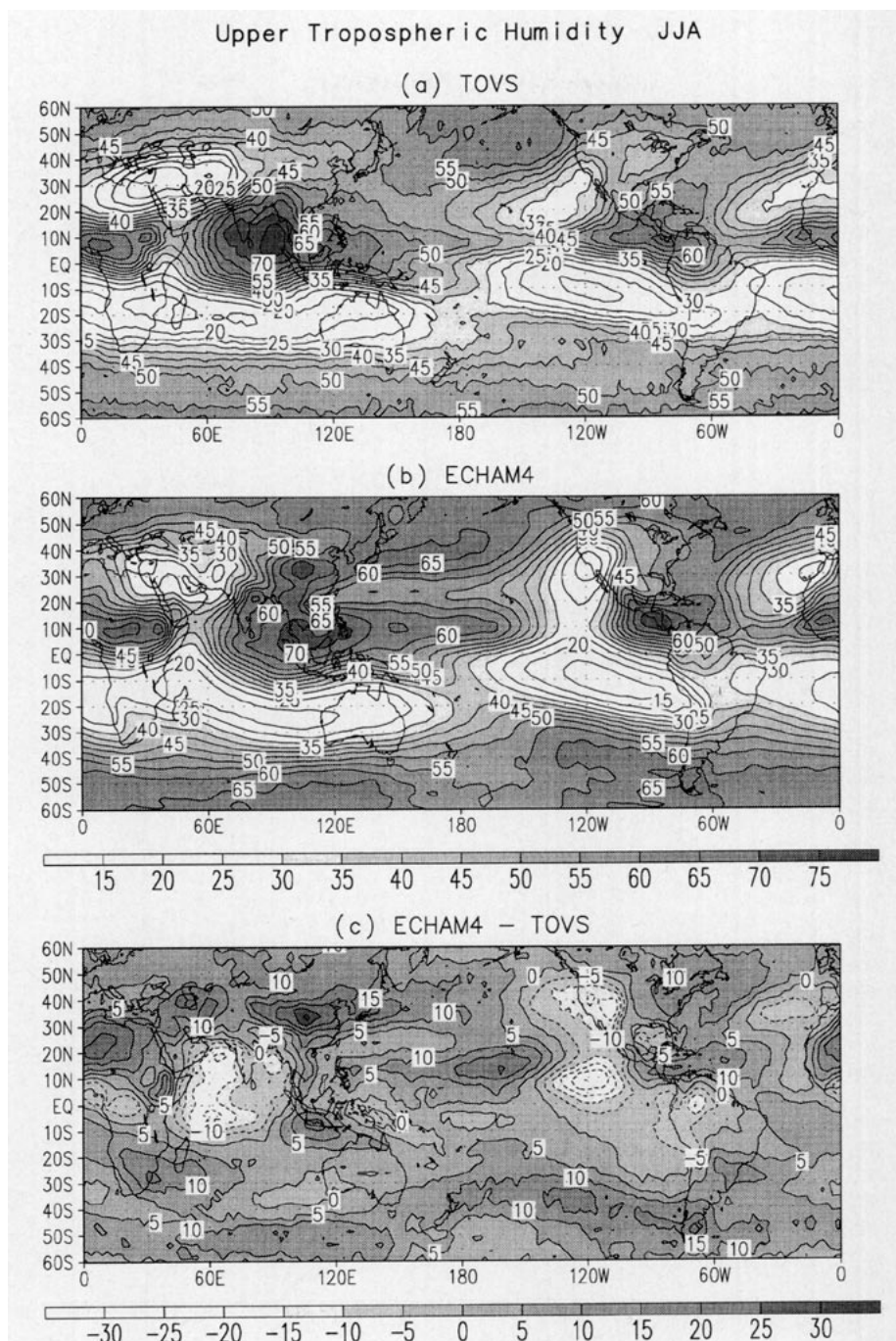
FIG. 8. Geographic distribution of the JJA seasonal mean UTH from (a) TOVS,
(b) ECHAM4, and (c) the difference ECHAM4-TOVS. Units are percent.

during the occurrence of specific phenomena (e.g., ENSO) is as important as the simulation of their mean fields and seasonal changes. Due to the limited time period of the satellite data used in this study, the comparison of TPW anomalies is done for the period between July 1987 and June 1991 (no SSM/I data in December 1987) and UTH anomalies for the period

between 1981 and 1988. For consistency, the anomalies in the model are calculated based on the same period as in the satellite measurements. Figure 11 shows the longitude–time (Hovmöller) diagram of SST anomalies near the equator (averaged from 5°N to 5°S) from 1979 to 1993. The SST anomalies are derived from the AMIP observed SST dataset, which was prescribed in
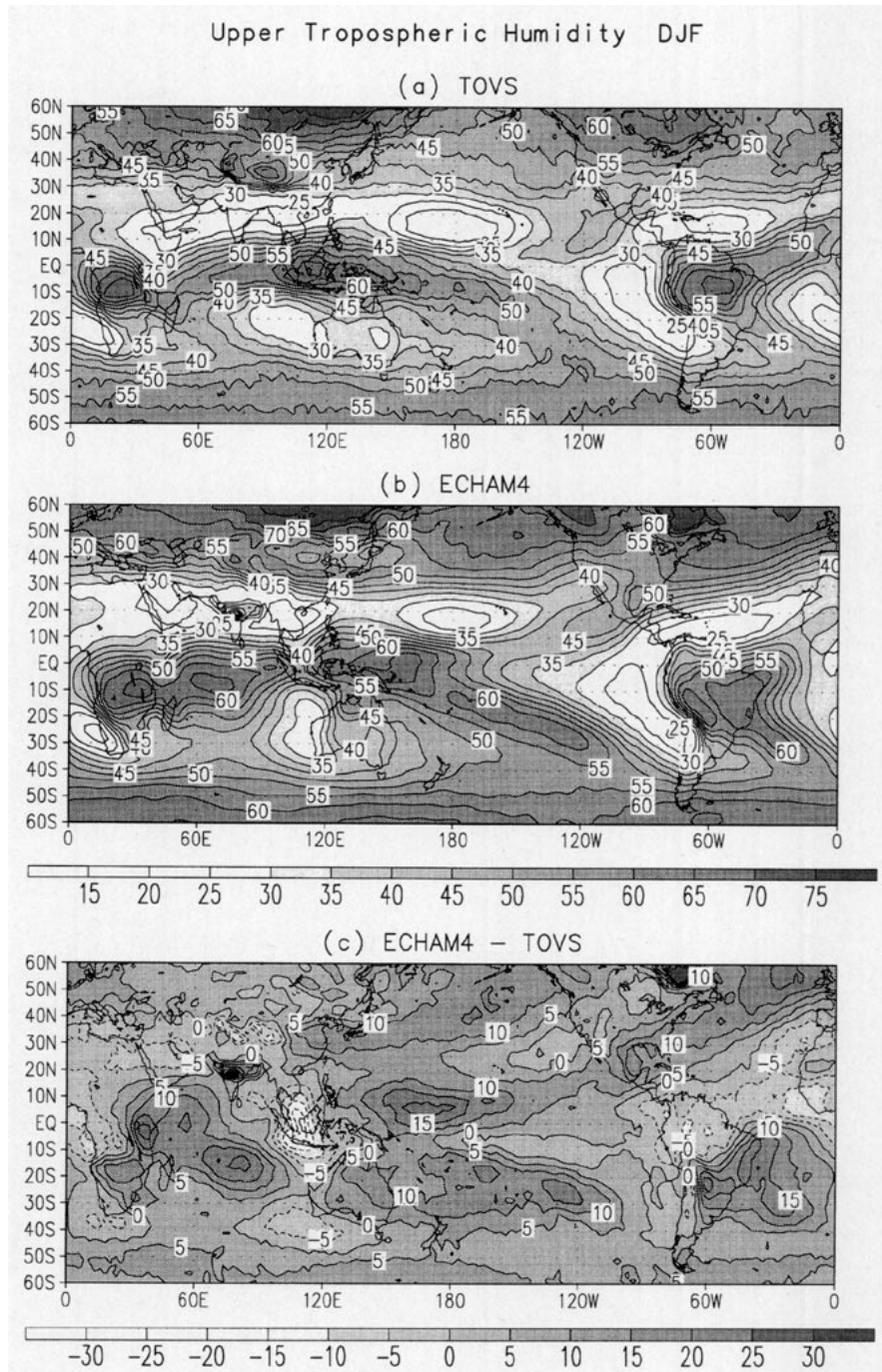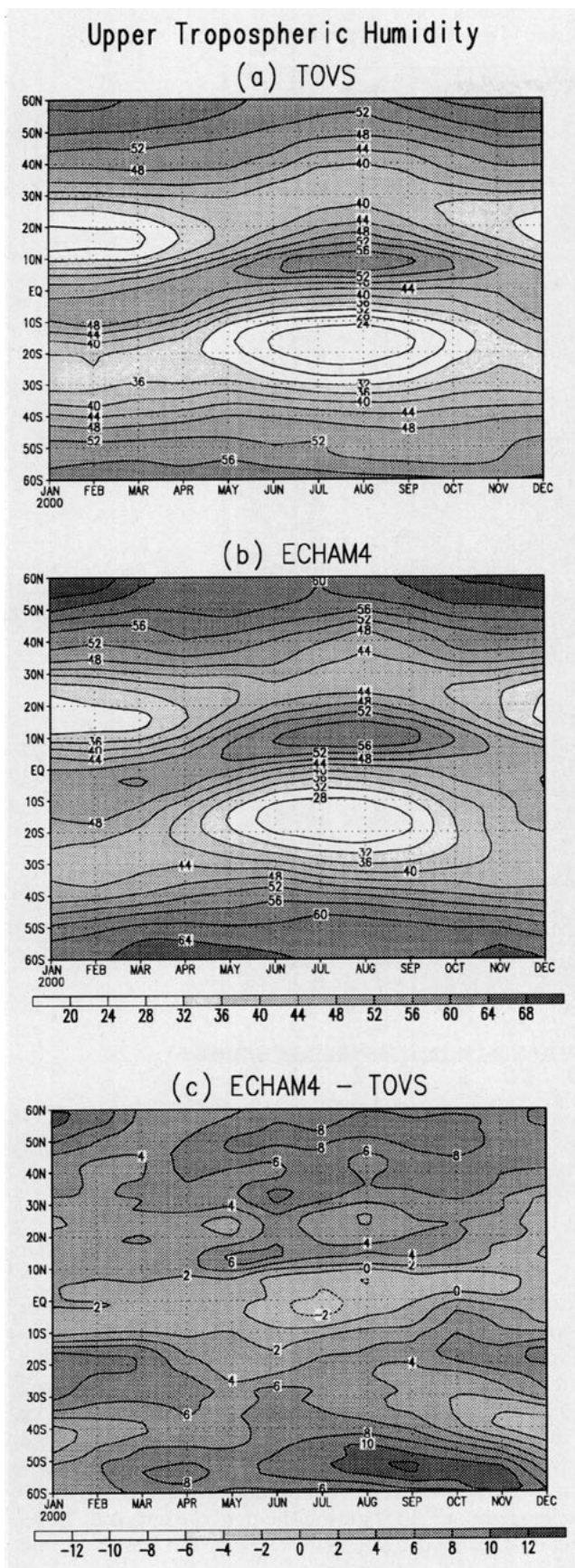
FIG. 9. As in Fig. 8 except for DJF season.

the model integration. Recent ENSO events are clearly illustrated. Below, the relationship between SST anomalies and water vapor anomalies are highlighted.

a. TPW

The equatorial TPW anomalies (averaged from 5°N to 5°S, over the ocean) from the 4-year SSM/I data are

shown in Fig. 12a. A 5-month running mean is applied to remove the small-scale noise. The effect of SST anomalies in 1987–1988 and 1988–1989 on the inter-annual variation in TPW along the equator circle is demonstrated. Thermodynamical impact on the tropical water vapor abundance is significant in terms of inter-annual timescale. A weak positive TPW anomaly in the Pacific Ocean is found in the early 1990. However, its

FIG. 10. Latitude–month distribution of the zonal mean UTH from (a) TOVS, (b) ECHAM4, and (c) the difference ECHAM4-TOVS. Units are percent.

relation to the SST anomaly is less obvious. In addition, while the large SST anomalies tend to occur east of the date line in the equatorial Pacific, the large TPW anomalies mostly develop near the date line. This is related to the anomalous low-level convergence generally found to the west of where the maximum SST gradient is situated (Lindzen and Nigam 1987; Barnett et al. 1991). These features demonstrate the dynamical influences on the spatial pattern of interannual variation in TPW. Influence from the interannual variation of the tropical circulation is clearly shown in the preferred location for extrema of equatorial TPW. The deep convection and moisture convergence, normally situated over the western Pacific and associated with the ascending branch of the Walker circulation, are shifted eastward over the warm SST in the central and eastern Pacific during the El Niño year (Webster 1983).

Figure 12b shows the equatorial TPW anomalies (averaged from 5°N to 5°S, over the ocean, and 5-month running mean) as simulated by ECHAM4. For the comparison in this section, the model integration is extended to cover the same time span as the SSM/I data. The opposite TPW anomalies during 1987–1988 El Niño and 1988–1989 La Niña, respectively, are captured by the model. The extreme TPW anomalies also develop near the date line. These characteristics reveal that the thermodynamical and dynamical influences on TPW are reasonably well simulated by ECHAM4. However, the positive anomalies over the equatorial Pacific in the first half of 1990 are also not as clearly reproduced in ECHAM4. Additionally, the magnitude of the anomalies in the model tend to be slightly larger than in the observations, possibly indicating that the model's moisture field is more sensitive to the prescribed SST anomalies. Indeed, the interannual variations in TPW seem to be more closely related to the SST anomalies in the model than in the observations.

b. UTH

The equatorial UTH anomalies derived from the 8-yr TOVS data is presented in Fig. 13a. As with TPW, the interannual variations in UTH are clearly influenced by the SST anomalies. Positive UTH anomalies form over the central and eastern Pacific during the 1982–1983 and 1987–1988 El Niño events. Since the SST does not have a direct link to the UTH as it does to the TPW, it is the change in the large-scale tropical circulation associated with the SST anomalies that is responsible for the UTH variations. The accompanied negative anomalies over the western Pacific warm pool during the El Niño events further affirm the expected
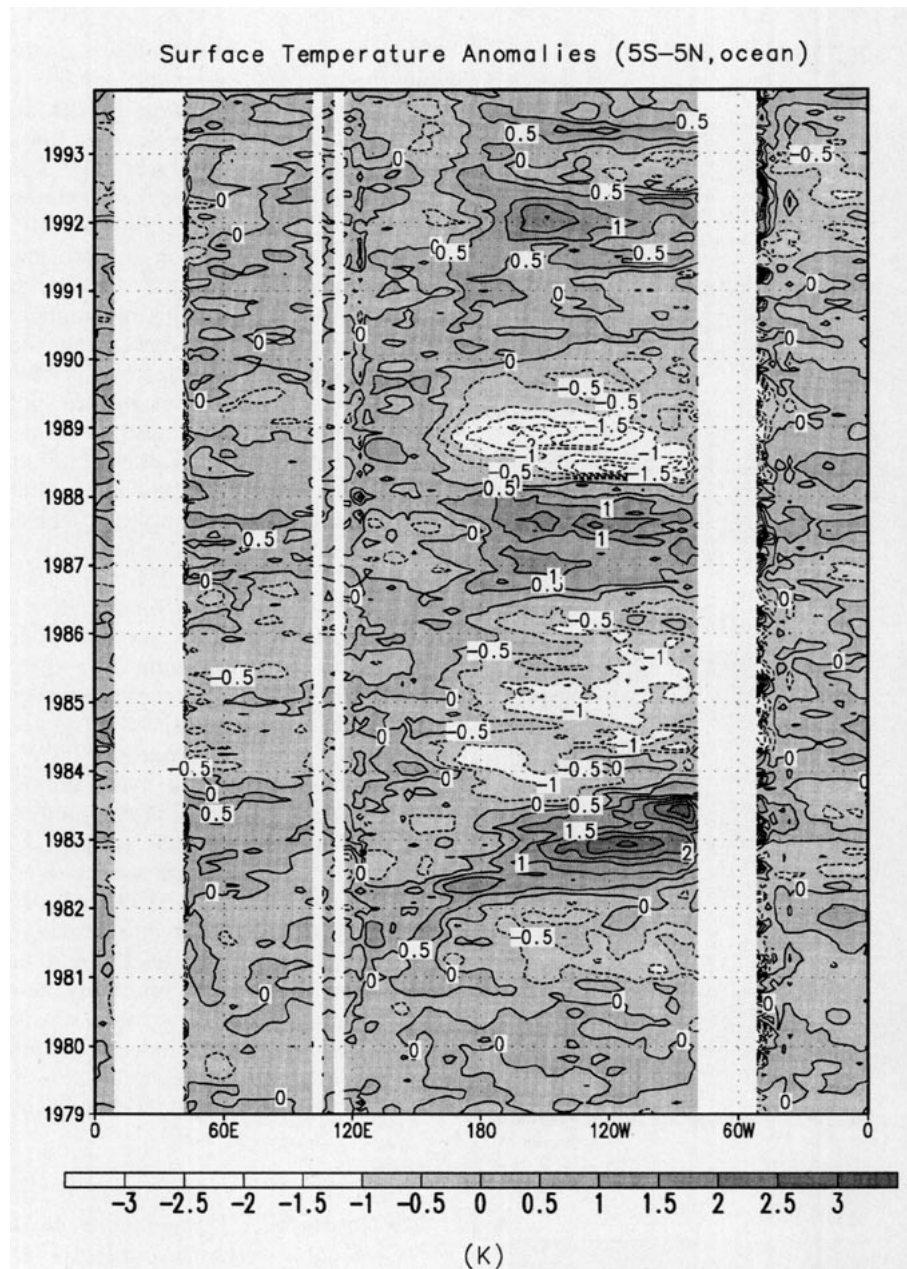
FIG. 11. Longitude–time distribution of the equatorial (averaged from 5°N to 5°S)
SST anomalies from AMIP dataset. Units are kelvins.

impact from the change in the Walker circulation along the equator.

Figure 13b presents a Hovmöller diagram of equatorial UTH anomalies simulated by ECHAM4. The temporal evolution of the UTH anomalies is reasonably well captured by the model; however, as with the TPW anomalies, the magnitude of the UTH anomalies is significantly overestimated. That is, the UTH anomalies are much more sensitive to the SST anomalies in the model than in TOVS observation. Again, these results

suggest changes in the tropical circulation and hydrological cycle under anomalous SST conditions are too vigorous in the model simulation, presumably caused by an overly sensitive convective scheme (Nordeng 1994). One should also note that a potential source of difference between the TOVS observation and ECHAM4 simulation is that the TOVS measurements may have intersatellite calibration anomalies due to the change in satellites during the period examined. However, the good agreement between the observed and ·
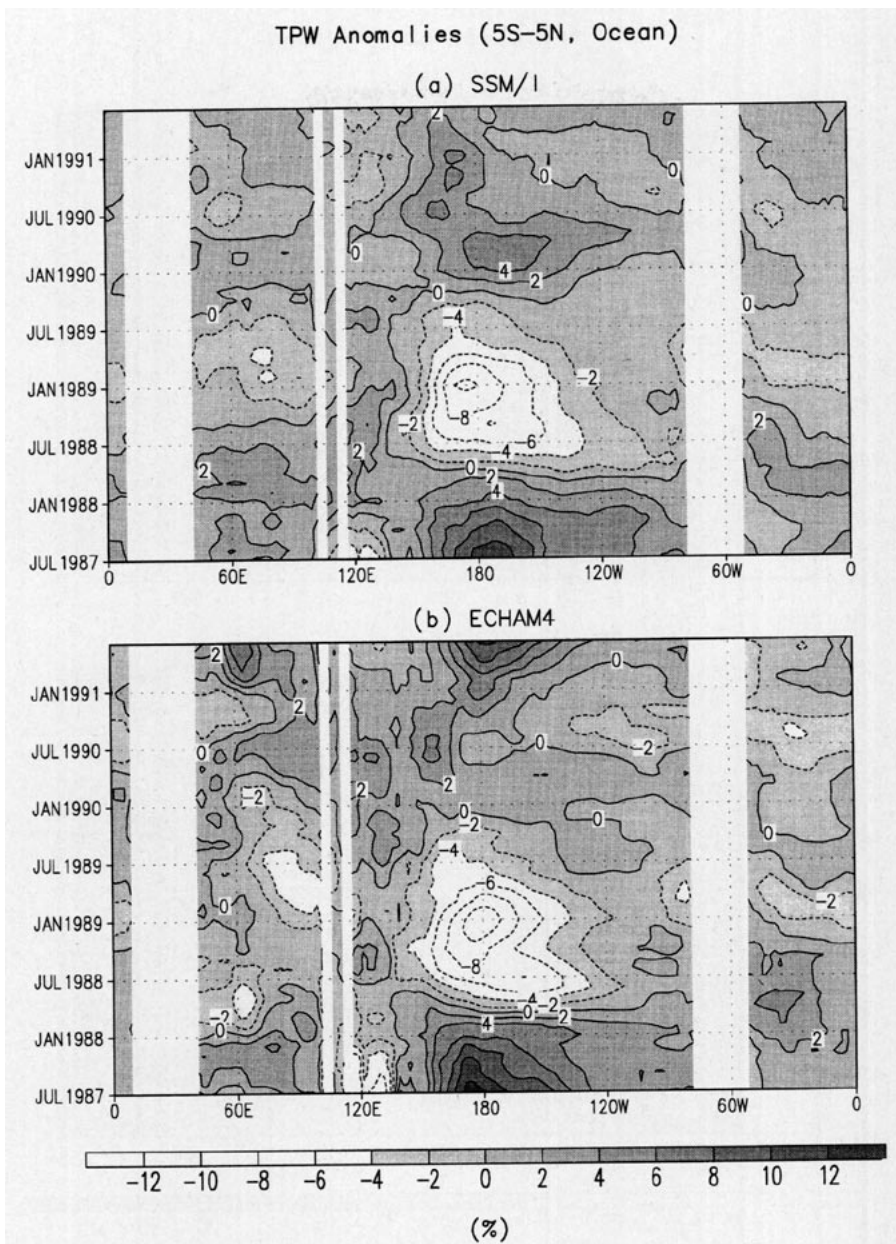
FIG. 12. Longitude–time distribution of the equatorial (averaged from 5°N to 5°S) TPW anomalies over the ocean from (a) SSM/I observations and (b) ECHAM4 simulations. Units are kilograms per square meter.

simulated fields suggests that the impact of the calibration differences upon the anomaly patterns is relatively small.

6. Water vapor distribution simulation using different physical parameterizations

There are many improvements in physical parameterization of various key climate processes in ECHAM4 as compared to the previous version

ECHAM3 (documented in Roeckner et al. 1992). The changes in water vapor advection scheme, parameterization of deep convection, subgrid-scale cloud formation, and others are expected to affect the water vapor distribution in the model. By comparing the TPW and UTH distribution from ECHAM3 and ECHAM4 integration, we attempt to highlight the impacts of these changes in physical parameterizations. One has to be cautious, however, in interpreting the results since different processes in the model interact and feedback on
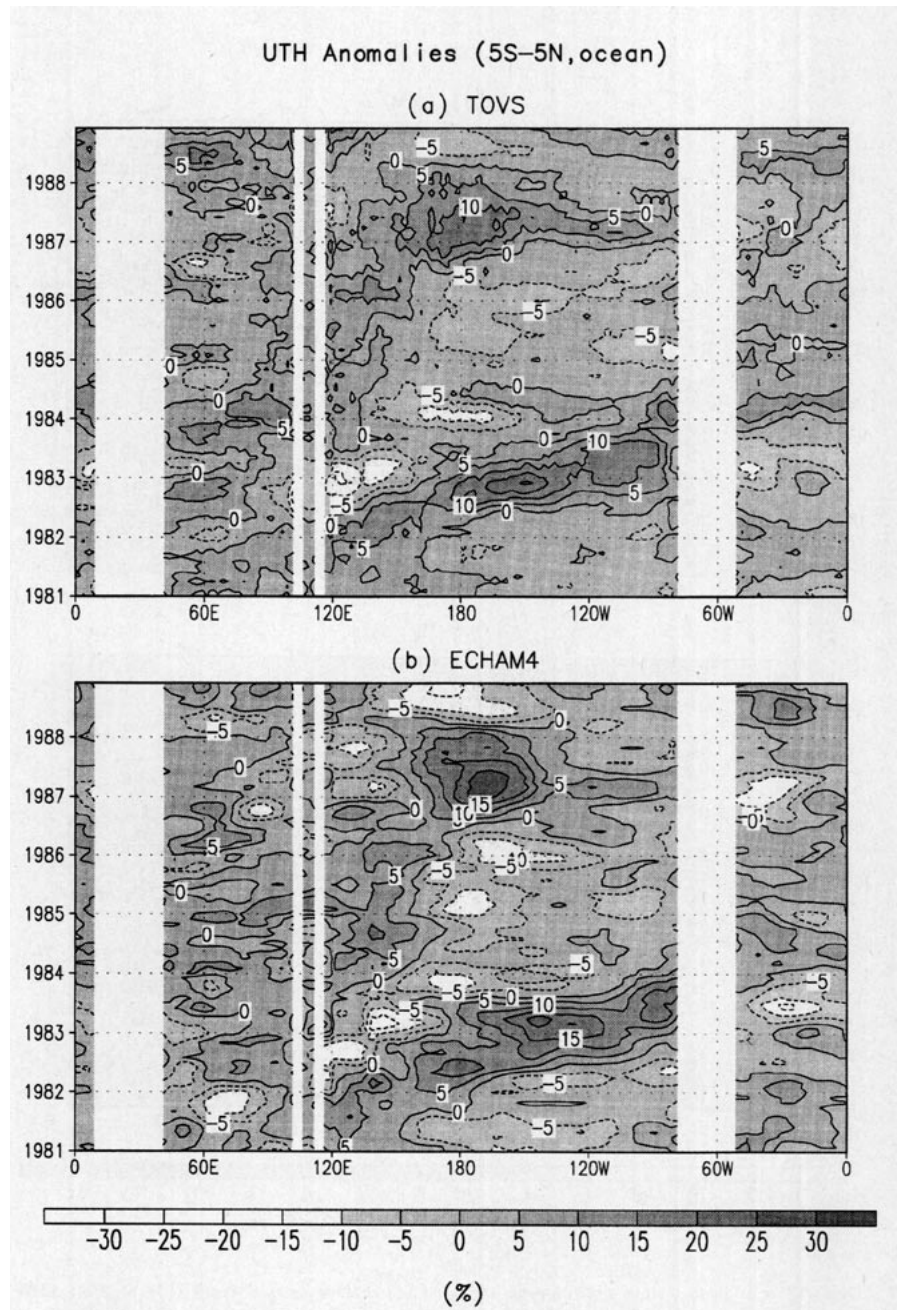
FIG. 13. Longitude–time distribution of the equatorial (averaged from 5°N to 5°S) UTH anomalies over the ocean from (a) TOVS observations, and (b) ECHAM4 simulations. Units are percent.

each other. As opposed to the ECHAM4 run, the ECHAM3 run uses a climatological annual cycle of SST derived from the AMIP SST dataset (1979–1988) for a 20-year integration. Thus, there is no interannual variability in the SST forcing for the ECHAM3 integration. Since we show only the ensemble mean water vapor climatology, this difference should not have a significant impact on the results.

Figure 14 shows the geographical distribution of annual mean TPW from ECHAM3 and differences from the SSM/I observation. The main features of the annual mean TPW associated with the tropical convergence zone and large-scale subsidence regions are also reasonably well simulated in ECHAM3. However, the discrepancies in ECHAM3 reveal interesting differences compared to those
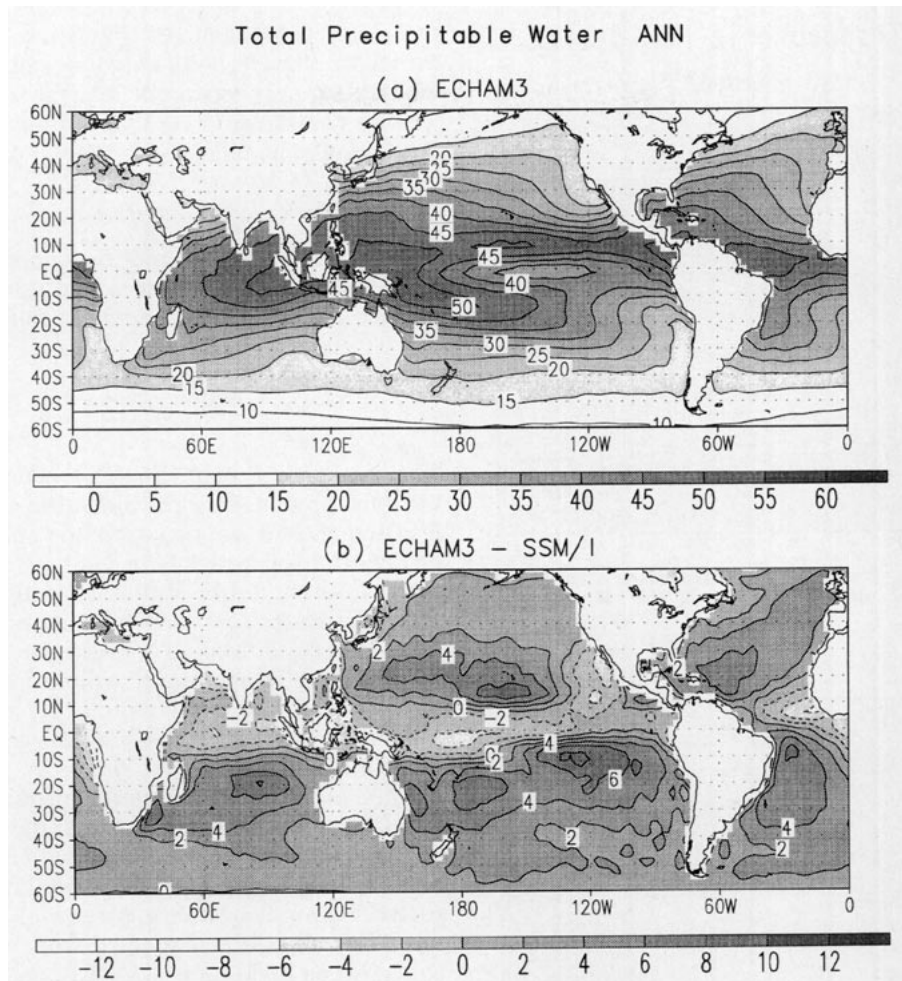
FIG. 14. Geographic distribution of the annual mean TPW from (a) ECHAM3 and
(b) the difference ECHAM3-SSM/I. Units are kilograms per square meter.

found in ECHAM4 (Fig. 1c). Some of these differences are directly linked to the changes in parameterizations. In ECHAM3 (Fig. 14b), there is a drier zone throughout the equatorial circle, while the nearby subtropical oceans are too moist and the locations of the ITCZ and SPCZ are shifted slightly poleward. There is also a stronger separation of the convection zone to the west of the date line (Fig. 14a). This discrepancy is related to the split ITCZ feature commonly found in GCMs that use moisture convergence closure for cumulus convection (Hess et al. 1993; Slingo et al. 1994). Due to the vanishing Coriolis parameter, frictional convergence cannot be maintained on the equator. Therefore, with relatively uniform moisture in the lower troposphere, the deep convection preferentially occurs off the equator (Slingo et al. 1994). However, with the new buoyancy closure for penetrative convection used in ECHAM4, this problem is less evident.

To demonstrate the impact of different physical parameterization on UTH, we discuss the seasonal cycle of the zonally averaged UTH from ECHAM3 and the difference with respect to the TOVS observations (Fig. 15). As in ECHAM4, the seasonal migration of the equatorial moist zone and the subtropical dry zone coincide with the movements of the ITCZ and large-scale subsidence areas associated with Hadley circulation. However, the off-equator preferential location of deep convection, as discussed above, broadens the area of high UTH. This feature persists throughout the year with largest biases found in the earlier months. ECHAM3 also underestimates the UTH in the boreal winter over higher latitudes. This discrepancy is likely related to the spectral water vapor advection scheme used in ECHAM3. The unphysical negative vapor amount and spurious condensation produced by the spectral scheme in the upper troposphere and polar
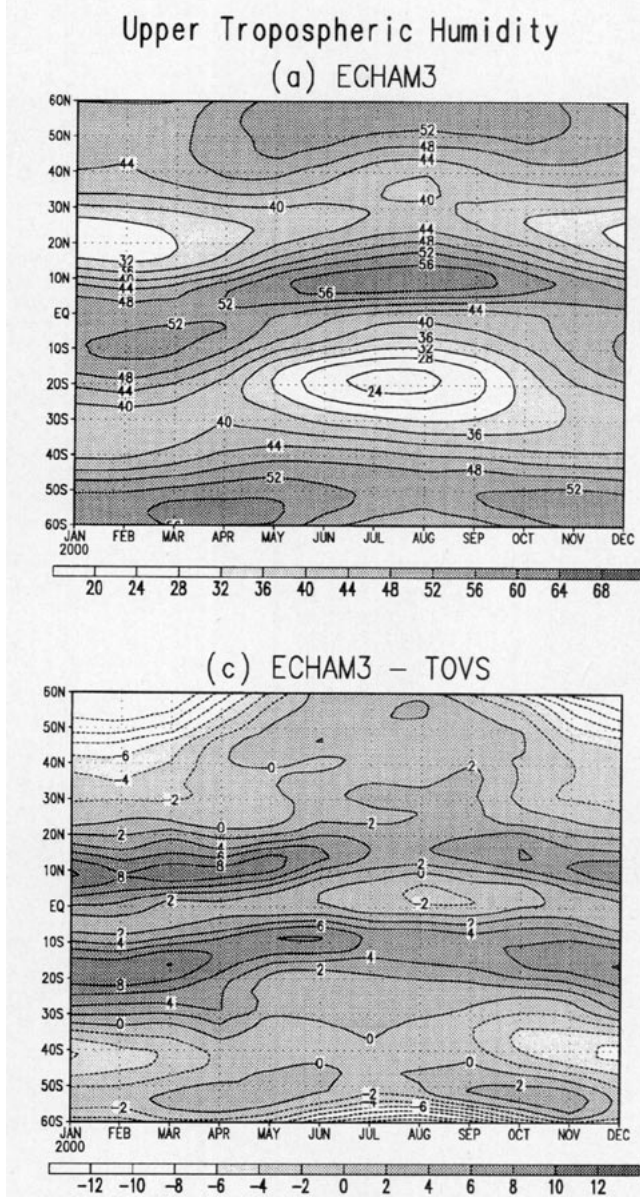
Upper Tropospheric Humidity

FIG. 15. Latitude–month distribution of the zonal mean UTH from (a) ECHAM3 and (b) the difference ECHAM3-TOVS. Units are percent.

region leads to this dry bias in UTH. Also, contrary to the seasonal cycle in TOVS observations (Fig. 10a), the simulated UTH is larger in boreal summer over the Northern Hemisphere midlatitudes (Fig. 15a). Since it uses a semi-Lagrangian transport scheme, this bias is not as apparent in the ECHAM4 simulations (Fig. 10c).

7. Impacts of water vapor simulation

In this section, we briefly examine the impact of errors in the simulated water vapor distribution upon other aspects of the model simulation. Two candidates for this are the clear-sky outgoing longwave radiation, which is strongly dependent upon the abundance of water vapor, and the cloud distribution, which depends upon relative humidity.

a. Clear-sky greenhouse effect

To examine the impact of the water vapor distribution upon the model's clear-sky OLR, we define a normalized greenhouse parameter G_{clr} following Stephens and Greenwald (1991):

$$G_{clr} = \frac{\sigma T_s^4}{OLR_{clr}}, \qquad (5)$$

where σ is the Stefan–Boltzman constant and T_s is the surface temperature. Since the OLR is always less than the surface emission, the greenhouse effect of the atmosphere leads to $G_{clr} > 1$. The OLR_{clr} is taken from the Earth Radiation Budget Experiment (ERBE; Barkstrom 1984) measurements under clear-sky conditions. To avoid the differences in land surface temperature, which are calculated in the model, we examine only the G_{clr} over the ocean. The prescribed SST is used for all greenhouse effect calculations.

The geographic distribution of the annual mean G_{clr} from ERBE, ECHAM4, and the differences in G_{clr} between ERBE and ECHAM4 are illustrated in Fig. 16. The pattern of the greenhouse effect from ERBE mainly follows the pattern of TPW observation. This should be expected from the direct linkage between SST, clear-sky OLR, and column moisture (Raval and Ramanathan 1989). In ECHAM4, the main pattern in the annual mean G_{clr} distribution is reasonably well simulated. However, there are notable errors in the simulated G_{clr} that are associated with the model biases in TPW and UTH. Specifically, smaller G_{clr} off the west coast of the continents, in the Bay of Bengal, and over the Arabian Sea likely stem from underpredictions in both TPW and UTH. Whereas the overestimate of G_{clr} over the Indian Ocean, off the southern Brazil coast, and over the central Pacific are associated with larger TPW and UTH. Additionally, the overestimate of G_{clr} in the midlatitudes is correlated with the overprediction of UTH.

Using scatterplots, Fig. 17 highlights the above model-observation differences in G_{clr} versus deficiencies in TPW and UTH simulations over two regions: (i) the Pacific storm track (25°–45°N and 120°E–180°) and (ii) the tropical eastern Pacific Ocean (5°S–25°N and 100°–140°W). Many model grid points have larger G_{clr} but negative bias in TPW over the Pacific storm track (Fig. 17a). These places, however, are normally accompanied by overestimates of UTH (Fig. 17b). Thus, in this region, model error in UTH plays a more dominant role in deter-
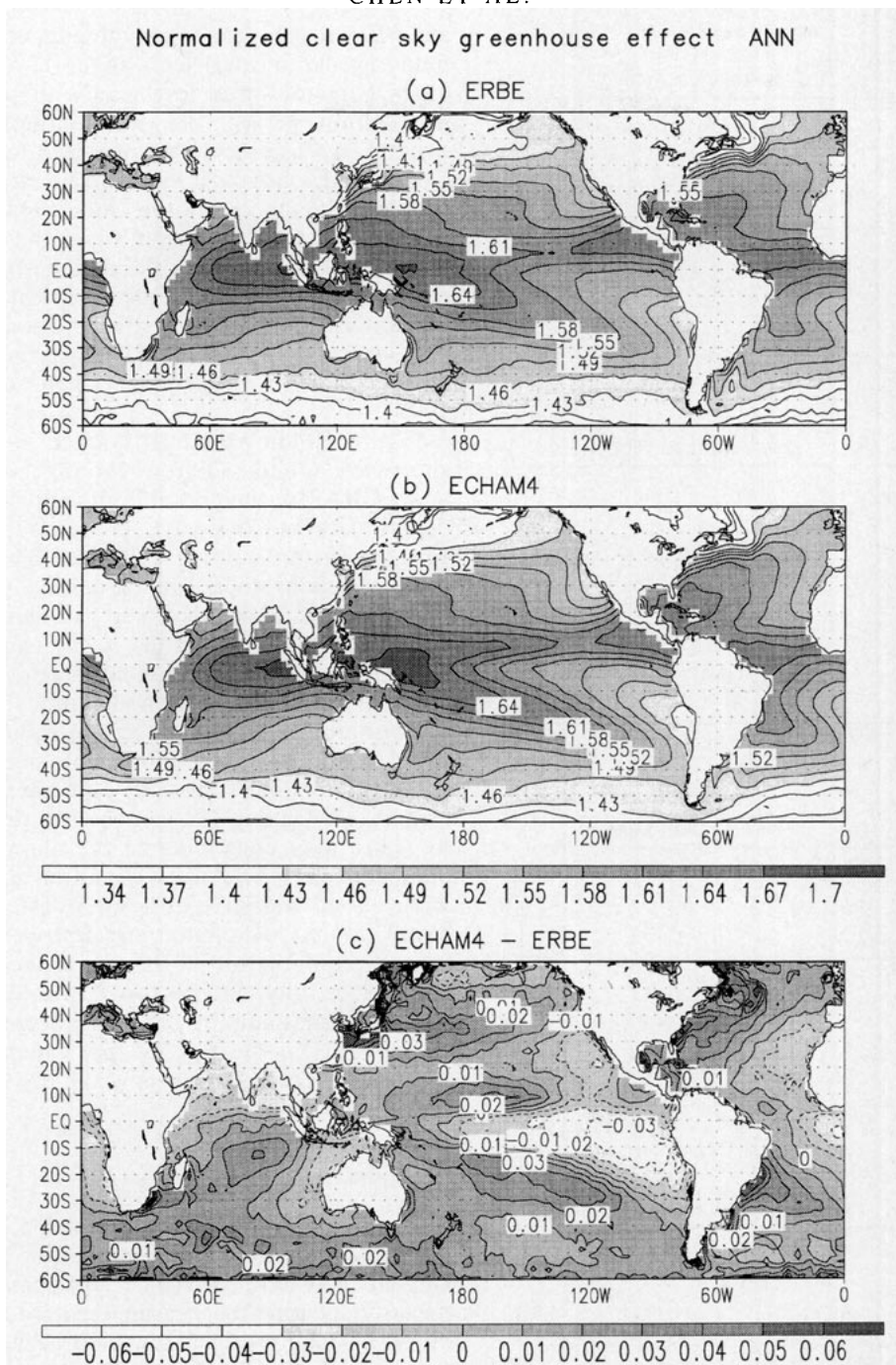
FIG. 16. Geographic distribution of the annual mean normalized clear-sky greenhouse effect from (a) ERBE, (b) ECHAM4, and (c) the difference ECHAM4–ERBE.

mining the differences in G_{clr}. On the other hand, ECHAM4 underestimates the G_{clr} for most of the tropical eastern Pacific Ocean where the simulated TPW exhibits a moist bias (especially for grids with larger negative biases in G_{clr}). This suggests that underestimates in UTH are compensating for the errors in TPW.

b. Cloud distribution

Cloud formation is strongly dependent upon the relative humidity predicted by the model. Here, we highlight some of the discrepancies in cloud simulation that could be related to the aforementioned errors in the water vapor distribution. Since consider-
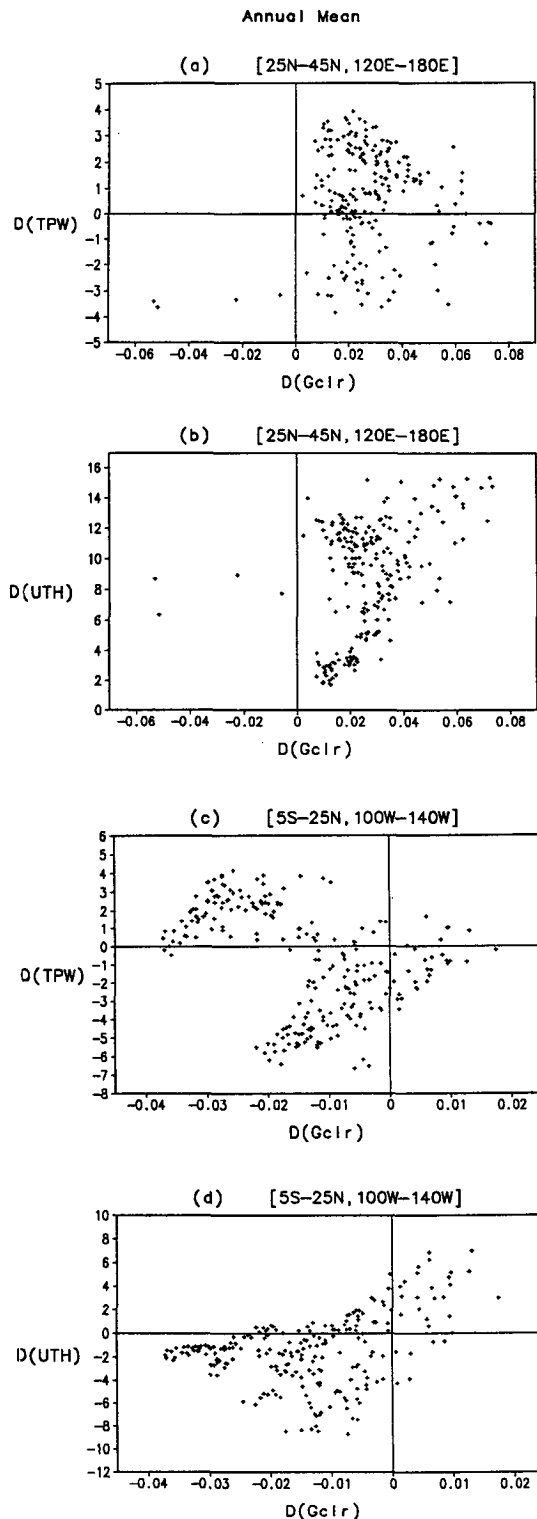
Annual Mean

FIG. 17. Differences (ECHAM4–ERBE) in the annual mean normalized clear-sky greenhouse effect G_{clr} versus (a) differences (ECHAM4–SSM/I) in TPW (kg m^{-2}) and (b) difference (ECHAM4–TOVS) in UTH (%) for the Pacific storm track region (25°–45°N, 120°E–180°). (c) and (d) As in (a) and (b) except for the tropical eastern Pacific Ocean region (5°S–25°N, 100°–140°W).

able differences are found among observed cloud fields (Mokhov and Schlesinger 1994), a reliable cloud climatology to test against the cloud vertical distribution is still not fully completed. Consequently, we use the cloud radiative forcing derived from ERBE observation as an indicator of possible problems in simulating the cloud fields and suggest connections with the water vapor biases. However, one should not interpret the deficiency in the cloud radiative forcing simulation as bias in the water vapor simulation alone, since discrepancies in the cloud forcing are also related to the parameterization of cloud radiative properties (Chen and Roeckner 1995).

Figure 18 shows the difference in annual mean shortwave cloud radiative forcing between ERBE and ECHAM4. One notable discrepancy is the underestimate in shortwave cloud radiative forcing over the eastern subtropical ocean. This bias results from an underprediction in marine stratocumulus cloud cover, which is likely associated with the model dry bias. Indeed the water vapor and cloud amount are both dependent upon achieving realistic simulations of the thermodynamic structure and mixing processes within the atmospheric boundary layer. In addition, the overestimate of tropical shortwave cloud radiative forcing coincides with areas of larger TPW and UTH, suggesting that the excess moisture may contribute to the anomolously high cloud cover. However, we caution that the shortwave cloud radiative forcing is affected by both cloud amount and cloud optical properties, and that it is the combination of the two aspects that lead to the final results. Studies on the impact of various cloud schemes and the different formulations of the hydrological cycle linking the water vapor, cloud water, and precipitation is a subject of further investigation.

8. Summary

The satellite measurements provide a unique data source for validating the water vapor distribution in GCMs. There have been some developments of various means to interpret the measured radiance to the desired physical quantities and to illustrate the interactions with the atmospheric circulation. Their application to the validation of the moisture fields and processes in climate models is invaluable since the traditional radiosonde climatologies have known limitations. In this study, we demonstrated that the chief patterns of geographical distribution and seasonal variation in the column moisture and relative humidity in the upper troposphere simulated in the ECHAM4 GCM are comparable with those inferred from satellite observations. The ability of the model to characterize the influence of dynamical processes on the water vapor distribution are also demonstrated. It is encouraging that the current
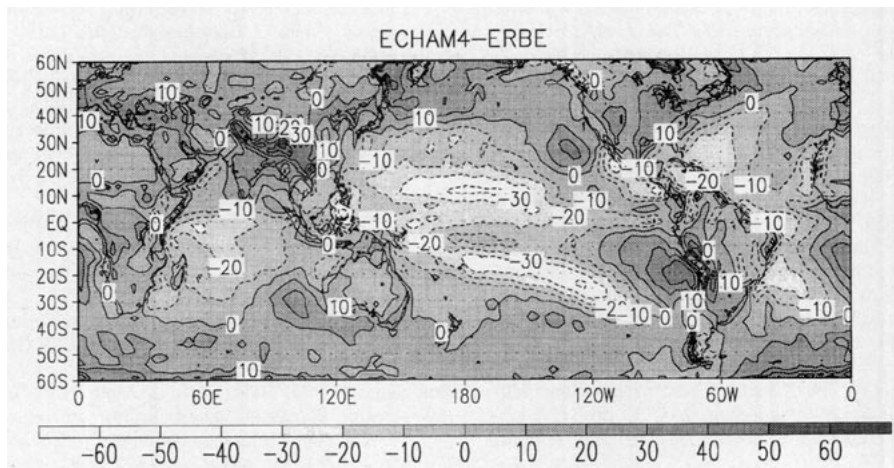
FIG. 18. Differences in the annual mean shortwave cloud radiative forcing
from ECHAM4–ERBE. Units are watts per square meter.

model fulfils these fundamental requirements for the climate simulation.

Although the water vapor distribution were reasonably well simulated in the model, some notable discrepancies were found. In particular, the models tended to underestimate the TPW over the eastern subtropical ocean in the summer hemisphere due to both enhanced anticyclonic circulations and stronger large-scale subsidence. The TPW over the western Pacific warm pool was also slightly reduced due to differences in the geographical location of the tropical convergence zones in ECHAM4. In the upper troposphere, excess UTH over the tropical convective centers and differences in the regional patterns of UTH were shown to be related to discrepancies in simulating the pattern and strength of the Walker circulation.

In addition to the time-mean moisture fields, the interannual variability of water vapor and its link with tropical SST anomalies were also in good qualitative agreement with the satellite observations. Changes in tropical circulation associated with ENSO events were clearly manifest in the simulated temporal evolution of the TPW and UTH anomalies. However, the moisture anomalies in the model tend to be more sensitive to the SST anomalies than the satellite observations indicate, especially for UTH.

We also compared the present results with simulations from a previous version of the ECHAM model (ECHAM3) to illustrate the impact of changes in the physical parameterizations upon the moisture distribution. A distinct improvement in the dry bias in UTH over the wintertime high latitudes in ECHAM4 likely results from the use of a semi-Lagrangian transport scheme for water vapor advection, while the change in convective parameterizations results in an improved simulation of TPW along the equator.

The discrepancies in simulating the water vapor distribution were also shown to be linked with errors in the simulated radiation budget. Specifically, the clear-sky greenhouse trapping was overestimated over areas with excessive TPW and UTH, and vice versa. It is possible that the underestimate of the marine stratocumulus over the eastern subtropical oceans is also related to the dry bias in the model. However, the cloud scheme involves a number of macro- and microphysical processes that can be affected by other factors. A natural extension of this study is to formulate sensitivity studies on the effect of various schemes used in different parts of hydrological cycle on water vapor climatology and variability. It would also be interesting to study not only the mean fields but also the processes (e.g., moisture transport) that contribute to the final water vapor distribution.

REFERENCES

Alishouse, J., C. S. A. Snyder, J. Vongasthorn, and R. R. Ferraro, 1990: Determination of oceanic total precipitable water from the SSM/I. *IEEE Trans. Geosci. Remote Sens.,* **28,** 811–816.
Barkstrom, B. R., 1984: The Earth Radiation Budget Experiment (ERBE). *Bull. Amer. Meteor. Soc.,* **65,** 1170–1185.
Barnett, T. P., M. Latif, E. Kirk, and E. Roeckner, 1991: On ENSO physics. *J. Climate,* **4,** 487–515.
Betts, A. K., 1990: Greenhouse warming and the tropical water vapor budget. *Bull. Amer. Meteor. Soc.,* **71,** 1465–1467.
Blondin, C., 1989: Research on land surface parameterization schemes at ECMWF. *Proc. of the Workshop on Parameterization of Fluxes Over Land Surface,* European Centre for Medium-Range Weather Forecasts, 285–330.

Brinkop, S., and E. Roeckner, 1995: Sensitivity of a general circulation model to parameterizations of cloud-turbulence interactions in the atmospheric boundary layer. *Tellus,* **47A,** 197–220.

Browning, K. A., 1994: Survey of perceived priority issues in the parameterizations of cloud-related processes in GCMs. *Quart. J. Roy. Meteor. Soc.,* **120,** 483–487.

Cess, R. D., and Coauthors, 1990: Intercomparison and interpretation of climate feedback processes in 19 atmospheric general circulation models. *J. Geophys. Res.,* **95,** 16 601–16 615.

Chahine, M. T., 1992: The hydrological cycle and its influence on climate. *Nature,* **359,** 373–380.

Chen, C.-T., and E. Roeckner, 1996: Validation of the earth radiation budget as simulated by the Max Planck Institute for Meteorology general circulation model ECHAM4 using satellite observations of the Earth Radiation Budget Experiment (ERBE). *J. Geophys. Res.,* **101,** 4269–4284.

Claussen, M., U. Lohmann, E. Roeckner, and U. Schulzweida, 1994: A global data set of land–surface parameterization. Max-Planck-Institut für Meteorologie Rep. 135, 30 pp. [Available from MPI für Meteorologie, Bundesstr. 55, D-20146 Hamburg, Germany.]

Dümenil, L., and E. Todini, 1992: A rainfall-runoff scheme for use in the Hamburg climate model. *Advances in Theoretical Hydrology, a Tribute to James Dooge,* European Geophysical Society Series of Hydrological Sciences, Vol. 1, Elsevier, 129–157.

Fouquart, Y., and B. Bonnel, 1980: Computations of solar heating of Earth's atmosphere: A new parameterization, *Beitr. Phys. Atmos.,* **53,** 35–62.

Gaffen, D. J., and T. P. Barnett, 1992: A comparison of observations and model simulations of tropospheric water vapor. *J. Geophys. Res.,* **97,** 2775–2780.

——, ——, and W. P. Elliot, 1991: Space and time scales of global tropospheric moisture. *J. Climate,* **4,** 989–1008.

Gates, W. L., 1992: AMIP: The Atmospheric Model Intercomparison Project. *Bull. Amer. Meteor. Soc.,* **73,** 1962–1970.

Giorgetta, M., and M. Wild, 1995: The water vapor continuum and its representation in ECHAM4. Max-Planck-Institut für Meteorologie Rep. 162, 38 pp. [Available from MPI für Meteorologie, Bundesstr. 55, D-20146 Hamburg, Germany.]

Hense, A., M. Kerschgens, and E. Raschke, 1982: An economical method for computing radiative transfer in circulation models. *Quart. J. Roy. Meteor. Soc.,* **108,** 231–252.

Hess, P. G., D. S. Battisti, and P. J. Rasch, 1993: The maintenance of the intertropical convergence zones and the large-scale tropical circulation on a water-covered earth. *J. Atmos. Sci.,* **50,** 691–713.

Lindzen, R. S., 1990: Some coolness concerning global warming. *Bull. Amer. Meteor. Soc.,* **71,** 288–299.

——, and S. Nigam, 1987: On the role of sea surface temperature gradients and forcing, low-level winds and convergence in the tropics. *J. Atmos. Sci.,* **44,** 2418–2436.

Liu, T. W., W. Tang, and F. Wentz, 1992: Precipitable water and surface humidity over global oceans for the SSM/I and ECMWF. *J. Geophys. Res.,* **97,** 2251–2264.

Lohmann, U., E. Roeckner, W. D. Collins, A. J. Heymsfield, G. McFarquhar, and T. P. Barnet E., 1995: The role of water vapor and convection during the Central Equatorial Pacific Experiment (CEPEX) from observation and model simulations. *J. Geophys. Res.,* in press.

Louis, J. F., 1979: A parametric model of vertical eddy fluxes in the atmosphere. *Bound.-Layer Meteor.,* **17,** 187–202.

Manabe, S., and R. T. Wetherald, 1967: Thermal equilibrium of the atmosphere with a given distribution of relative humidity. *J. Atmos. Sci.,* **24,** 241–259.

Miller, M. J., A. C. M. Beljaars, and T. N. Palmer, 1992: The sensitivity of the ECMWF model to the parameterization of evaporation from tropical oceans. *J. Climate,* **5,** 418–434.

Mokhov, I. I., and M. E. Schlesinger, 1994: Analysis of global cloudiness. 2. Comparison of ground-based and satellite-based cloud climatologies. *J. Geophys. Res.,* **99,** 17 045–17 065.

Morcrette, J.-J., 1991: Radiation and cloud radiative properties in the European Centre for Medium-Range Weather Forecasts forecasting system. *J. Geophys. Res.,* **96,** 9121–9132.

Nordeng, T. E., 1994: Extended versions of the convective parameterization scheme at ECMWF and their impact on the mean and transient activity of the model in the tropics. European Centre for Medium-Range Weather Forecasts Research Department Tech. Memo. 206, 41 pp. [Available from ECMWF, Shinfield Park, Reading/Berkshire RG2 9AX, United Kingdom.]

Olson, J. S., J. A. Watts, L. J. Allison, 1983: Carbon in live vegetation of major world ecosystems. ORNL-5862, Environmental Sciences Division Publ. 1997, Oak Ridge National Laboratory, Oak Ridge, TN.

Oort, A. H., 1983: Global atmospheric circulation statistics, 1958–1973. NOAA Professional Paper 14, U.S. Government Printing Offices, Washington, DC, 180 pp.

Prabhakara, C., G. Dalu, R. C. Lo, and N. R. Nath, 1979: Remote sensing of seasonal distribution of precipitable water over the oceans and the inference of boundary layer structure. *Mon. Wea. Rev.,* **107,** 1388–1401.

Rasch, P. J., and D. L. Williamson, 1991: The sensitivity of a general circulation model climate to the moisture transport formulation. *J. Geophys. Res.,* **96,** 13 123–13 137.

Raval, A., and V. Ramanathan, 1989: Observational determination of the greenhouse effect. *Nature,* **342,** 758–762.

Reynolds, R. W., 1982: A monthly averaged climatology of sea surface temperature. NOAA Tech. Rep. NWS 31, National Weather Service, Silver Spring, MD, 35 pp.

Rockel, B., E. Raschke, and B. Weyres, 1991: A parameterization of broad band radiative transfer properties of water, ice and mixed clouds. *Beitr. Phys. Atmos.,* **64,** 1–12.

Roeckner, E., M. Rieland, and E. Keup, 1991: Modelling of cloud and radiation in the ECHAM model. *ECMWF/WCRP Workshop on Clouds, Radiative Transfer and the Hydrological Cycle,* Reading, United Kingdom, European Centre for Medium-Range Weather Forecasts, 199–222.

——, K. Arpe, L. Bengtsson, S. Brinkop, L. Dümenil, M. Esch, E. Kirk, F. Lunkeit, M. Ponater, B. Rockel, R. Sausen, U. Schlese, S. Schubert, M. Windelband, 1992: Simulation of the present-day climate with the ECHAM model: Impact of model physics and resolution. Max-Planck-Institut für Meteorologie, Report No. 93, 171 pp. [Available from MPI für Meteorologie, Bundesstr. 55, D-20146 Hamburg, Germany.]

Rossow, W. B., and A. A. Lacis, 1990: Global, seasonal cloud variation from satellite radiance measurements. Part II: Cloud properties and radiative effects. *J. Climate,* **3,** 1204–1253.

Salathé, E. P., Jr., and D. Chesters, 1995: Variability of moisture in the upper troposphere as inferred from TOVS satellite observation and ECMWF model analyses in 1989. *J. Climate,* **8,** 120–132.

Slingo, J. M., M. Blackburn, A. Betts, R. Brugge, K. Hodges, B. Hoskins, M. Miller, L. Steenman-Clark, and J. Thuburn, 1994: Mean climate and transience in the tropics of the UGAMP GCM: Sensitivity to convective parameterization. *Quart. J. Roy. Meteor. Soc.,* **120,** 881–922.

Soden, B. J., and F. P. Bretherton, 1993: Upper tropospheric relative humidity from the GOES 6.7-μm channel: Method and climatology for July 1987. *J. Geophys. Res.,* **98,** 16 669–16 688.

——, and ——, 1994: Evaluation of water vapor distribution in general circulation models using satellite observation. *J. Geophys. Res.,* **99,** 1187–1210.

——, and R. Fu, 1995: A satellite analysis of deep convection, upper tropospheric humidity and the greenhouse effect. *J. Climate,* **8,** 2333–2351.

——, and J. R. Lanzante, 1996: An assessment of satellite and radiosonde climatologies of upper tropospheric water vapor. *J. Climate,* **9,** 1235–1250.

Stephens, G. L., 1990: On the relationship between water vapor over the ocean and sea surface temperature. *J. Climate,* **3,** 634–645.

——, and T. J. Greenwald, 1991: The earth's radiation budget and its relation to atmospheric hydrology. 1. Observations of the clear sky greenhouse effect. *J. Geophys. Res.,* **96,** 15 311–15 324.

Sun, D.-Z., and R. S. Lindzen, 1993: Distribution of tropical tropospheric water vapor. *J. Atmos. Sci.,* **50,** 1643–1660.

Sundquist, H., 1978: A parameterization scheme for nonconvective condensation including prediction of cloud water content. *Quart. J. Roy. Meteor. Soc.,* **104,** 677–690.

Tiedtke, M., 1989: A comprehensive mass flux scheme for cumulus parameterization in large scale models. *Mon. Wea. Rev.,* **117,** 1779–1800.

Walcek, C. J., 1994: Cloud cover and its relationship to relative humidity during a springtime midlatitude cyclone. *Mon. Wea. Rev.,* **122,** 1021–1035.

Waliser, D. E., and C. Gautier, 1993: A satellite-derived climatology of the ITCZ. *J. Climate,* **6,** 2162–2174.

Webster, P. J., 1983: The large-scale structure of the tropical atmosphere. *Large-Scale Dynamical Processes in the Atmosphere,* B. J. Hoskins and R. Pearce, Eds., Academic Press, 235–276.

Weinreb, M. P., H. E. Fleming, L. M. McMillin, and A. C. Neuendorffer, 1981: Transmittances for the TIROS Operational Vertical Sounder. NOAA Tech. Rep. NESS 85, 66 pp.

Williamson, D. L., and P. J. Rasch, 1989: Two dimensional semi-Lagrangian transport with shape preserving interpolation. *Mon. Wea. Rev.,* **117,** 102–129.

——, and ——, 1994: Water vapor transport in the NCAR CCM2. *Tellus,* **46A,** 34–51.

Wu, X., J. J. Bates, and S. J. S. Khalsa, 1993: A climatology of the water vapor band brightness temperatures from NOAA Operational satellites. *J. Climate,* **6,** 1282–1300.

Xu, K. M., and S. K. Krueger, 1991: Evaluation of cloudiness parameterization using a cumulus ensemble model. *Mon. Wea. Rev.,* **119,** 342–367.